Isotropic and Azimuthally Anisotropic Rayleigh Wave Dispersion Across the Juan de Fuca and Gorda Plates and U.S. Cascadia from Earthquake Data and Ambient Noise Two- and Three-Station Interferometry

Shane Zhang*[1], Hongda Wang[1], Mengyu Wu[1], and Michael H. Ritzwoller[1]

[1] Department of Physics, University of Colorado Boulder, Boulder, CO 80309, USA.

Abstract

We use data from the Cascadia Initiative (CI) amphibious array and the USArray Transportable Array to construct and compare Rayleigh wave isotropic and azimuthally anisotropic phase speed maps across the Juan de Fuca and Gorda Plates extending onto the continental northwestern U.S. Results from both earthquakes (28–80 s) as well as ambient noise two- and three-station interferometry (10–40 s) are produced. Compared with two-station interferometry, three-station direct wave interferometry provides $> 50\%$ improvement in the signal-to-noise ratio (SNR) and the number of dispersion measurements obtained particularly in the noisier oceanic environment. Earthquake and ambient noise results are complementary in bandwidth and azimuthal coverage, and agree within about twice the estimated uncertainties of each method. We, therefore, combine measurements from the different methods to produce composite results that provide an improved data set in accuracy, resolution, and spatial and azimuthal coverage over each individual method. A great variety of both isotropic and azimuthally anisotropic structures are resolved. Across the oceanic plate, fast directions of anisotropy with 180° periodicity (2ψ) generally align with paleo-spreading directions while 2ψ amplitudes mostly increase with lithospheric age, both displaying substantial variations with depth and age. Strong ($> 3\%$) apparent anisotropy with 360° periodicity (1ψ) is observed at long periods (> 50 s) surrounding the Cascade Range, probably caused by backscattering from heterogeneous isotropic structures.

Key words: Seismic anisotropy; Seismic interferometry; Seismic noise; Seismic tomography; Structure of the Earth; Surface waves and free oscillations.

*shzh3924@colorado.edu

1 Introduction

Large earthquakes ($M_w \geq 8$) have recurred in Cascadia with a period of ∼500 years over the last 10,000 years (e.g. Atwater, 1987; Goldfinger et al., 2012), and the most recent one is dated to the 1700s (e.g. Nelson et al., 1995; Satake et al., 1996). Motivated by the capability of $M_w \sim 9$ earthquakes on the Cascadia subduction zone, the Cascadia Initiative (CI, Toomey et al., 2014) deployed an array of ocean-bottom seismographs (OBS) and land stations spanning from the Juan de Fuca and Gorda Ridges onto the continent in the northwestern U.S. The CI array also provides an opportunity to image the Juan de Fuca Plate from formation to subduction, which may shed light on the thermal state, hydration and melt extent of the oceanic plate (e.g. Tian et al., 2013; Bell et al., 2016; Eilon and Abers, 2017; Rychert et al., 2018; Ruan et al., 2018; Janiszewski et al., 2019), cooling (e.g. Byrnes et al., 2017; Janiszewski et al., 2019) and deformation (e.g. Martin-Short et al., 2015; Bodmer et al., 2015; VanderBeek and Toomey, 2017; VanderBeek and Toomey, 2019) of the oceanic lithosphere, structure of the Locked and Transition Zones along the Cascadia margin (e.g. Hawley et al., 2016; Bodmer et al., 2018), and subduction of the oceanic plate (e.g. Janiszewski and Abers, 2015; Gao, 2016; Hawley and Allen, 2019). Furthermore, structual studies can provide constraints for hazard analysis, such as using the downdip limits of the subducted plate to constrain how close source zones are to metropolitan areas (Hyndman and Wang, 1993).

Classical two-station ambient noise interferometry (e.g. Campillo and Paul, 2003; Shapiro and Campillo, 2004) extracts information about the medium between two synchronous receivers, which leads to ambient noise tomography (e.g. Shapiro et al., 2005; Sabra et al., 2005). In contrast, three-station interferometry (e.g. Stehly et al., 2008; Curtis and Halliday, 2010), based on two-station interferograms, additionally can bridge *asynchronously* deployed receivers (e.g. Ma and Beroza, 2012; Curtis et al., 2012). Furthermore, three-station direct-wave interferometry is recently shown to produce substantial improvement in Rayleigh wave dispersion measurements across the western U.S. (Zhang et al., 2020), and potentially may be useful in this noisier amphibious setting. In addition, previous studies predominantly use earthquake body waves to observe azimuthal anisotropy on the Juan de Fuca and Gorda Plates (e.g. Martin-Short et al., 2015; Bodmer et al., 2015; VanderBeek and Toomey, 2017; VanderBeek and Toomey, 2019).

Our two principal purposes of this study are (1) to investigate the performance of three-station direct-wave interferometry and (2) to produce Rayleigh wave isotropic and azimuthal anisotropy observations from both earthquakes and ambient noise across the Juan de Fuca and Gorda plates extending onto the continent. We use the CI array and some regional seismic networks for Rayleigh wave observations from two-station interferometry, three-station interferometry, and earthquake data. The final product is a set of Rayleigh wave azimuthally anisotropic phase speed maps across the Cascadia combining ambient noise and earthquake observations.

First, three-station direct-wave interferometry has been tested in the western U.S. and is found to produce higher SNR dispersion measurements, to bridge asynchronously deployed stations, and to derive isotropic phase speed maps consistent with two-station interferometry (Zhang et al., 2020). However, the quality of two-station interferograms there is already quite high. Thus, we address the extent of improvement from three-station interferometry in this noisier amphibious setting with less ideal station geometry. Moreover, we test if azimuthal anisotropy observations from three-station interferometry are also consistent with two-station interferometry. To validate the noise-based results, we introduce earthquake data as independent observations. Janiszewski et al. (2019) find significant discrepancies ($> 3\%$) in Rayleigh wave isotropic phase speed maps across Cascadia derived from two-station interferometry and earthquakes, especially near the coastline (some locations $> 10\%$). As we will show, differences between earthquake and noise-based results are reduced ($< 1\%$) by using a different methodology, especially after denoising OBS data.

Second, to date azimuthal anisotropy on the Juan de Fuca and Gorda Plates has been predominantly observed from earthquake body waves (e.g. Martin-Short et al., 2015; Bodmer et al., 2015; VanderBeek and Toomey, 2017; VanderBeek and Toomey, 2019) and appears challenging to observe from earthquake surface waves (Bell et al., 2016; Eilon and Forsyth, 2020). We show robust observations of azimuthal anisotropy from earthquake surface waves based on eikonal (Lin et al., 2009) and Helmholtz tomography (Lin and Ritzwoller, 2011b). We also present Rayleigh wave azimuthal anisotropy measurements and tomographic maps from ambient noise two- and three-station interferometry which, to the best of our knowledge, have not been produced offshore. In obtaining the 2ψ azimuthal anisotropy results, we pay attention to observing and correcting for the effect of apparent 1ψ azimuthal anisotropy, which may be caused by strongly heterogeneous isotropic structures and may bias 2ψ anisotropy measurements (e.g. Lin and Ritzwoller, 2011a).

The paper is structured as follows. First, we describe the processing of data for ambient noise two-station and three-station direct-wave interferometry and for earthquake observations, including the denoising of OBS data and the de-biasing of three-station interferometry (**section 2**). Next, we measure Rayleigh wave dispersion from the different methods and compare their characteristics, contrasting the quality of measurements based on OBS and land stations (**section 3**). Next, we quantify the differences in the phase speed maps from the different methods utilizing the estimated uncertainties (**section 4**). Finally, by combining results from the different methods we construct composite maps for both isotropic and azimuthally anisotropic structure (**section 5**).

2 Data processing

The stations used in this work extend from the Juan de Fuca and Gorda Ridges onto the continent in the northwestern U.S. The resulting station set has an average spacing of ∼70 km (**Fig. 1a**). The total number of stations is 612 with 41% (252) Ocean Bottom Seismographs (OBS) and 59% (360) land stations. The stations are largely composed of the oceanic and the continental components of the Cascadia Initiative (CI). The CI OBS deployment is divided into four yearly phases from 2011-2014: most OBS are on the Juan de Fuca Plate in 2011 and 2013 while most are on the Gorda Plate in 2012 and 2014. The CI OBS are augmented with limited term deployments of OBS near the Blanco Transform Fault (2012 to 2013, Nabelek and Braunmiller, 2012) and on the Gorda Plate (2013 to 2015, Nabelek and Braunmiller, 2013). About 44% (157) of land stations are from the USArray Transportable Array (TA), most of which are deployed from 2005 to 2008 and are asynchronous with the CI stations.

2.1 Ambient noise data

To obtain information about the medium between two receivers, we apply both two-station ambient noise interferometry (e.g. Shapiro and Campillo, 2004; Shapiro et al., 2005) as well as three-station interferometry (e.g. Stehly et al., 2008; Curtis and Halliday, 2010; Zhang et al., 2020). We refer to interferograms from these methods generally as noise-based data, although three-station methods considered here primarily utilize the direct-wave part of two-station interferograms. In addition to cross-correlation, data processing to construct two-station interferograms includes denoising OBS data to reduce tilt and compliance noise, and temporal and spectral normalizations to reduce effects from uneven noise source distributions (**section 2.1.1**). Additionally, computation of three-station interferograms requires particular attention to choosing appropriate weights for each source-station, selecting either correlation or convolution depending on station geometry, and de-biasing to produce correct dispersion measurements (**section 2.1.2**).

The following is a summary of the notation used to describe the various interferometric methods (Zhang et al., 2020) used in this study:

- $\mathcal{I}_2^{AN}$: Two-station ambient noise interferometry.
- ${}^{ell}\mathcal{I}_3^{DW}$: Three-station direct-wave interferometry with source-stations in the elliptical stationary phase zone between the receiver stations.
- ${}^{hyp}\mathcal{I}_3^{DW}$: Three-station direct-wave interferometry with source-stations in the hyperbolic stationary phase zones radially outside the receiver stations.

2.1.1 Two-station interferometry

For $\mathcal{I}_2^{AN}$, the preprocessing of continuous data is performed in two major steps. First, we reduce tilt and compliance noise from vertical components of OBS using the horizontal components and the pressure gauges, respectively (e.g. Webb and Crawford, 1999; Crawford and Webb, 2000; Bell et al., 2015; Tian and Ritzwoller, 2017), in a process we refer to as "denoising". The denoising is particularly impactful at periods > 10 s and for shallow water OBS (Tian and Ritzwoller, 2017). Second, we apply traditional ambient noise pre-processing steps including temporal and spectral normalizations (Bensen et al., 2007; Ritzwoller and Feng, 2019, e.g.) to reduce the effects of strong directionally-dependent sources (such as earthquakes). Then the data are correlated and stacked over days to produce correlations between all synchronously deployed station-pairs. The correlations from nearby stations (distance < 0.5 km) are simply superimposed (stacked), whether the stations are deployed synchronously or not. Finally, we average the causal and acausal lags of the correlations to form the symmetric component, which we also use as the basis for three-station interferometry (**section 2.1.2**) and for tomography based on two-station interferometry (**section 4**).

2.1.2 Three-station interferometry

We first summarize the essentials of the three-station methods used in this study (**Fig. 2**) because three-station interferometric methods are currently less well established than two-stations methods. Zhang et al. (2020) presents the methods, notation, and terminology in detail. Consider three stations at a time, and denote two of them as receiver-stations, r_i, r_j, and the third as a source-station, s_k. The two two-station interferograms between s_k and r_i as well as s_k and r_j individually are correlated or convolved again to produce a source-specific three-station interferogram, $C_3(r_i, r_j; s_k)$, where C represents either correlation or convolution and the dependence on time is suppressed here. Then the source-specific interferograms are phase shifted and stacked over N source-stations with appropriate weights, $w_{ij;k}$, to produce the composite estimated Green's function, $\hat{G}_3$, between receiver-stations r_i and r_j:

$$\hat{G}_3(r_i, r_j) \equiv \sum_{k=1}^{N} w_{ij;k} \tilde{C}_3(r_i, r_j; s_k), \tag{1}$$

where $\tilde{C}_3$ denotes the interferogram C_3 after a "de-biasing" phase shift is applied. $\hat{G}_3$ provides information about the medium between receiver-stations r_i and r_j, which may be deployed asynchronously. Each weight w (indices suppressed) can be decomposed into three factors:

$$w = \mathbf{1}_{\text{geometry}} \cdot \mathbf{1}_{\text{SNR}} \cdot w_{\text{RMS}}, \tag{2}$$

where $\mathbf{1}_{\text{geometry}}$ is an indicator function that is 1 if s_k satisfies a particular geometrical constraints and 0 otherwise, $\mathbf{1}_{\text{SNR}}$ is also an indicator function that is 1 only if the SNR of both $\mathcal{I}_2(r_i, s_k)$ and $\mathcal{I}_2(r_j, s_k)$ are > 10. SNR is defined as the ratio between the peak amplitude in the signal window and the RMS of trailing noise (Bensen et al., 2007) throughout this study. w_{RMS} equals the reciprocal of the RMS of the trailing noise in the interferogram $\tilde{C}_3$, which normalizes amplitudes of $\tilde{C}_3$ while accentuating $\tilde{C}_3$ with high SNR.

The most fundamental component of the weight function is the geometrical weight, $\mathbf{1}_{\text{geometry}}$, which requires source-stations to lie within stationary phase zones (**Fig. 2**). To define the stationary phase zones, let d denote the great-circle distance between two stations, then let ${}^{hyp}\delta d$ represent the difference between the differential source-receiver distances and the inter-receiver distance (**Fig. 2a**):

$$ {}^{hyp}\delta d_{ij;k} = |d_{ki} - d_{kj}| - d_{ij}, \tag{3}$$

and let ${}^{ell}\delta d$ represent the difference between the sum of source-receiver distances and the inter-receiver distance (**Fig. 2b**):

$$ {}^{ell}\delta d_{ij;k} = |d_{ki} + d_{kj}| - d_{ij}, \tag{4}$$

corresponding to the methods ${}^{hyp}\mathcal{I}_3^{DW}$ and ${}^{ell}\mathcal{I}_3^{DW}$, respectively. Because of the triangle inequality, ${}^{hyp}\delta d \leq 0$ while ${}^{ell}\delta d \geq 0$. For both ${}^{hyp}\mathcal{I}_3^{DW}$ and ${}^{ell}\mathcal{I}_3^{DW}$, the stationary phase zones are *ad hoc* defined as

$$ |\delta d_{ij;k}| < \alpha \cdot d_{ij}, \tag{5}$$

with appropriate left superscripts for δd in eqs. (3) and (4). The stationary phase zones defined here do not depend on frequency, and we empirically choose $\alpha = 1\%$. For ${}^{ell}\mathcal{I}_3^{DW}$, the stationary phase zone is an ellipse, and $\mathcal{I}_2(r_i, s_k)$ and $\mathcal{I}_2(r_j, s_k)$ are convolved. For ${}^{hyp}\mathcal{I}_3^{DW}$, the stationary phase zone is a hyperbola, and $\mathcal{I}_2(r_i, s_k)$ and $\mathcal{I}_2(r_j, s_k)$ are correlated. Because signals in $\mathcal{I}_2^{AN}$ become unreliable for inter-station distances less than one wavelength λ, we also require both source-receiver distances to be greater than λ. For simplicity, but without rejecting too many source-stations, we use a cutoff wavelength at the longest period of interest:

$$ \min(d_{ki}, d_{kj}) > \lambda_{\max}, \tag{6}$$

where $\lambda_{\max} = 120$ km for a period of 40 s and an approximate wave speed of 3 km/s.

Without accounting for δd, the dispersion measurements will be biased. Zhang et al. (2020) presents a de-biasing scheme to measure the dispersion of each source-specific interferogram (C_3) individually with the corrected distance, $d_{ij} + \delta d_{ij;k}$. Then the source-specific dispersion curves are averaged over source-stations s_k with the standard deviation as an estimate of uncertainty. Here, in contrast, we present a new de-biasing approach in which we apply a phase shift to each original C_3 in the frequency domain:

$$ \tilde{C}_3 = \mathcal{F}^{-1}\left[\mathcal{F}[C_3] \cdot e^{i\omega\delta d/c}\right], \tag{7}$$

where $\mathcal{F}$ and $\mathcal{F}^{-1}$ denote the Fourier transform and its inverse, respectively, and c is an input estimate of phase speed between the receiver-stations. The dependence of C_3 and $\tilde{C}_3$ on r_i, r_j, s_k and time is suppressed for clarity in the preceding equation. **Fig. 3** shows an example of the effect of the phase shift for station triplets with different values of δd. For the method ${}^{hyp}\mathcal{I}_3^{DW}$ a phase delay is applied because ${}^{hyp}\delta d \leq 0$, while for the method ${}^{ell}\mathcal{I}_3^{DW}$ a phase advance is applied because ${}^{ell}\delta d \geq 0$.

The major difference in the three-station methods between this work and Zhang et al. (2020) is that here we apply a phase shift to de-bias. The main advantage of the phase shift approach is to preserve the stack of source-specific interferograms ($\hat{G}_3$), which is designed to produce more reliable dispersion measurements with broader bandwidth than the individual C_3. However, application of the phase shift requires prior knowledge of the phase speed, although the process can be iterated. In this study, we use prior information from phase speed maps constructed using $\mathcal{I}_2^{AN}$. Because we find the de-biasing effective (**section 4.1**), we do not iteratively update the phase speed map and re-apply the correction.

In Zhang et al. (2020), three-station coda-wave interferometry (e.g. Stehly et al., 2008) is also investigated and is found to produce lower SNR and more band-limited measurements than the methods $\mathcal{I}_2^{AN}$, ${}^{ell}\mathcal{I}_3^{DW}$ and ${}^{hyp}\mathcal{I}_3^{DW}$. In fact, we find coda-wave interferometry even more challenging in this noisy oceanic setting, so we do not present results from it here. Hence, when we refer to three-station methods here, we will mean three-station *direct-wave* interferometry.

2.2 Earthquake data

More than 2500 teleseismic earthquakes with $M_s > 5.5$ are used (**Fig. 1b**) to produce Rayleigh wave dispersion measurements. The earthquakes are widely distributed in azimuth with a predominant fraction from the western Pacific, which can provide complementary azimuthal coverage to noise-based data (**section 4**). Preprocessing of earthquake data recorded on OBS includes reducing tilt and compliance noise, similar to the denoising of ambient noise data recorded on OBS (**section 2.1.1**).

3 Dispersion measurements

We apply frequency-time analysis (e.g. Dziewonski et al., 1969; Levshin and Ritzwoller, 2001) to measure Rayleigh wave phase speed, assuming the instantaneous phase of the signal at frequency ω and time t to be (e.g. Lin et al., 2008):

$$\phi(\omega, t) = \omega\frac{d}{c} - \omega t + \frac{\pi}{4} + 2N\pi + \phi_s, \tag{8}$$

where d is the inter-receiver distance, c is the phase speed we wish to measure, $N \in \mathbb{Z}$, and ϕ_s is a source-dependent term. As discussed in detail by Zhang et al. (2020), an appropriate ϕ_s must be chosen to obtain approximately unbiased dispersion measurements for the different methods we consider here:

$$\phi_s = \begin{cases} 0 & \text{for } \mathcal{I}_2^{\mathrm{AN}}, \\ \pi/4 & \text{for } {}^{ell}\mathcal{I}_3^{\mathrm{DW}}, \\ -\pi/4 & \text{for } {}^{hyp}\mathcal{I}_3^{\mathrm{DW}}. \end{cases} \tag{9}$$

For earthquake data, ϕ_s will depend on source parameters and frequency, but here we simply choose $\phi_s = 0$ because only unbiased travel time *differences* are used in the tomography methods applied in this study (**section 4**). Differencing of phase travel time measurements approximately cancels the initial phase term. We also resolve 2π ambiguity for each earthquake by iteratively applying corrections to stations in order of increasing distance from the center station (Lin and Ritzwoller, 2011b). Similarly, one could also choose any constant as ϕ_s for the methods $\mathcal{I}_2^{AN}$, ${}^{ell}\mathcal{I}_3^{DW}$, and ${}^{hyp}\mathcal{I}_3^{DW}$ to perform tomography, although the dispersion measurements would be biased. Earthquake dispersion measurements from the TA stations are based on Shen and Ritzwoller (2016).

The source strengths with ambient noise and data quality can be cumulatively characterized by SNR. **Fig. 4a** shows the median of SNR versus period from all paths. On average, the SNR for the three-station measurements are about 50% higher than for the two-station measurements. SNR values are similar between the methods ${}^{ell}\mathcal{I}_3^{DW}$ and ${}^{hyp}\mathcal{I}_3^{DW}$. SNR curves for ambient noise-based data peak near the primary ($\sim$16 s) and secondary ($\sim$8 s) microseisms and decay rapidly at longer periods. The primary and secondary microseisms may be generated from different mechanisms (e.g. Tian and Ritzwoller, 2015). In contrast, the SNR curve for earthquakes shows a single peak around 35 s period and remains high (> 25) at longer periods but decays rapidly at shorter periods. Therefore, ambient noise and earthquake data complement each other by providing higher SNR measurements for periods below and above 30 s, respectively. The paths for noise-based data can are divided into three categories (**Figs 4b-d**) by the type of station-pair used: "Land-Land" (between land stations), "OBS-Land" (between OBS and land stations), and "OBS-OBS" (between OBS and OBS).

For Land-Land paths (**Fig. 4b**), the SNR is the highest among all categories. Three-station methods (${}^{ell}\mathcal{I}_3^{DW}$ and ${}^{hyp}\mathcal{I}_3^{DW}$) enhance SNR by an additive value of $\sim$10 compared with two-station interferometry ($\mathcal{I}_2^{AN}$), except for periods < 10 s. The enhancement is not large because the SNR of $\mathcal{I}_2^{AN}$ is already quite high (> 20) across a broad frequency band on land.

For OBS-Land paths (**Fig. 4c**), the SNR of $\mathcal{I}_2^{AN}$ peaks near 18 s period ($\sim$24) and decreases quickly at shorter and longer periods (< 10 at 40 s). On average, the SNR is more than three times lower than Land-Land paths (**Fig. 4a**). Because SNR of $\mathcal{I}_2^{AN}$ is low in the oceans, three-station methods ${}^{ell}\mathcal{I}_3^{DW}$ and ${}^{hyp}\mathcal{I}_3^{DW}$ provide substantial enhancements that nearly double the SNR of $\mathcal{I}_2^{AN}$.

For OBS-OBS paths (**Fig. 4d**), the SNR is the lowest among all categories of paths and drops quickly at periods > 12 s. SNR curves for the methods $\mathcal{I}_2^{AN}$ and ${}^{ell}\mathcal{I}_3^{DW}$ are very similar at periods > 12 s whereas ${}^{ell}\mathcal{I}_3^{DW}$ has a lower SNR at shorter periods. SNR curves for $\mathcal{I}_2^{AN}$ and ${}^{hyp}\mathcal{I}_3^{DW}$ are similar at periods < 12 s, whereas ${}^{hyp}\mathcal{I}_3^{DW}$ nearly doubles the SNR of $\mathcal{I}_2^{AN}$ at longer periods. The enhancement from ${}^{hyp}\mathcal{I}_3^{DW}$ compared with $\mathcal{I}_2^{AN}$ is important for obtaining more dispersion measurements as is discussed below. The method ${}^{hyp}\mathcal{I}_3^{DW}$ yields higher SNR than ${}^{ell}\mathcal{I}_3^{DW}$ because of the geometry of the methods (**Fig. 2**) and that OBS are noisier than land stations. Specifically, source-stations lie between the receiver-stations for ${}^{ell}\mathcal{I}_3^{DW}$, so all source-stations are OBS for OBS-OBS paths. In contrast, source-stations are in the end-fire directions for ${}^{hyp}\mathcal{I}_3^{DW}$, which could include land stations.

The quality control of the dispersion measurements includes two principal criteria. First, for both earthquake and ambient noise-based data, a spectral SNR threshold is applied that rejects a dispersion measurement at any period with SNR < 10. This SNR criterion rejects 20% to 50% of data for $\mathcal{I}_2^{AN}$, 10% to 30% for ${}^{ell}\mathcal{I}_3^{DW}$ and ${}^{hyp}\mathcal{I}_3^{DW}$, and 15% to 25% for earthquake data. Second, for noise-based data, a measurement at a given period is discarded if the inter-receiver distance is less than the wavelength at that period. This distance criterion only rejects a few percent of data.

Figs 4e-h show the number of paths after quality control versus period. In eikonal tomography, a single travel time measurement between two stations is used twice because each station can serve as a source and a receiver. For example, a travel time measurement between stations A and B yields two paths: from station A to station B and vice versa. Therefore, for the ambient noise methods, the number of paths are twice the number of measurements. In contrast, this doubling does not affect earthquake measurements; the number of paths and the number of travel time measurements are the same.

Fig. 4e shows the total number of paths from each method. Because SNR plays an important role in quality control, the number of paths varies with period similar to SNR (**Fig. 4a**). ${}^{ell}\mathcal{I}_3^{DW}$ and ${}^{hyp}\mathcal{I}_3^{DW}$ produce similar numbers of measurements with $\mathcal{I}_2^{AN}$ at periods < 10 s, but provide 50% to 100% more than $\mathcal{I}_2^{AN}$ at longer periods because of higher SNR as well as bridging asynchronously deployed stations. At long periods, earthquake data provide complementary paths to noise-based data. For this part of the discussion, we continue to label paths from noise-based data into three categories by whether OBS or land stations are involved as in **Figs 4b-d**.

For the Land-Land category (**Fig. 4f**), the method ${}^{ell}\mathcal{I}_3^{DW}$ produces a similar number of measurements to $\mathcal{I}_2^{AN}$ while the method ${}^{hyp}\mathcal{I}_3^{DW}$ produces $\sim$20% more paths at periods > 10 s. The method ${}^{hyp}\mathcal{I}_3^{DW}$ produces more measurements than ${}^{ell}\mathcal{I}_3^{DW}$ although their SNR's are similar (**Fig. 4b**), indicating that the station configuration is preferable for ${}^{hyp}\mathcal{I}_3^{DW}$. The Land-Land category composes 30% to 40% of all paths.

For the OBS-Land category (**Fig. 4g**), the methods ${}^{ell}\mathcal{I}_3^{DW}$ and ${}^{hyp}\mathcal{I}_3^{DW}$ produce $\sim$50% and $\sim$80% more measurements than $\mathcal{I}_2^{AN}$, respectively. The method ${}^{ell}\mathcal{I}_3^{DW}$ yields more measurements than ${}^{hyp}\mathcal{I}_3^{DW}$ although their SNR's are comparable (**Fig. 4c**), indicating that the station geometry is more advantageous for ${}^{ell}\mathcal{I}_3^{DW}$. About 50% of all paths are from the OBS-Land category.

For the OBS-OBS category (**Fig. 4h**), the method ${}^{ell}\mathcal{I}_3^{DW}$ produces a similar number of measurements as $\mathcal{I}_2^{AN}$ while ${}^{hyp}\mathcal{I}_3^{DW}$ produces several times more at periods > 10 s. The method ${}^{hyp}\mathcal{I}_3^{DW}$ yields more measurements than ${}^{ell}\mathcal{I}_3^{DW}$ because of much higher SNR (**Fig. 4d**). As discussed above, ${}^{hyp}\mathcal{I}_3^{DW}$ has higher SNR because of the geometrical constraints on the methods such that more land source-stations are included in this category for ${}^{hyp}\mathcal{I}_3^{DW}$ than for ${}^{ell}\mathcal{I}_3^{DW}$, and land stations have better signal quality than OBS. The OBS-OBS category constitutes the least of all paths among the three categories ($< 15\%$).

4 Comparing results from different methods

Combining the different types of data from different methods (two- and three-station interferograms, earthquake measurements) promises to reduce uncertainties, to enhance azimuthal coverage, and to broaden the bandwidth. However, the combination requires the data to be mutually consistent. In this section we test the hypothesis that the results from the different methods are consistent, and present a quantitative comparison of results for both isotropic (**section 4.2**) and azimuthally anisotropic properties (**section 4.3**). Ultimately, as we show, this comparison justifies the combination of the data sets. We discuss the composite isotropic and anisotropic phase speed maps in **section 5**.

4.1 Methodology, notation, and terminology

We perform Helmholtz tomography (Lin and Ritzwoller, 2011b) for earthquake data and eikonal tomography (Lin et al., 2009) for ambient noise data. We do not use more traditional integrated ray tomographic methods (e.g. Barmin et al., 2001) for comparing results from different data because they usually require tuning of regularization parameters in an ad hoc way depending on the path distribution. The results from traditional methods with different numbers of measurements, therefore, are difficult to compare with one another. Furthermore, Helmholtz/eikonal tomography yields local estimates of uncertainties, which are useful to guide the comparison of different methods and are crucial for studies based on phase speed maps (e.g. 3-D inversions for both isotropic and anisotropic structures).

A single mode and single frequency surface wave approximately satisfies the 2-D homogeneous wave equation (e.g. Lin et al., 2012). Assuming a sufficiently smooth Earth model and ignoring local amplifications, separation of variables yields:

$$\frac{1}{c_i^2(\boldsymbol{r})} = |\nabla \tau_i(\boldsymbol{r})|^2 - \frac{\nabla^2 A_i(\boldsymbol{r})}{\omega^2 A_i(\boldsymbol{r})}, \tag{10}$$

which uses the travel time, τ_i, and amplitude, A_i, from the ith (virtual or real) source to estimate source-specific corrected (or structural) phase speed, c_i, at the location $\boldsymbol{r}$. Helmholtz tomography is based on eq. (10) and is a finite frequency method.

If the amplitude field is sufficiently smooth or the frequency is high then the second term on the RHS of eq. (10) will be small compared to the first term, which produces the eikonal equation:

$$\frac{\hat{k}_i(\boldsymbol{r})}{c_i'(\boldsymbol{r})} \cong \nabla\tau_i(\boldsymbol{r}), \tag{11}$$

where $\hat{k}_i$ is ray propagation direction and c_i' is apparent (or dynamic) phase speed. Eikonal tomography is based on eq. (11) and is a geometrical ray theoretic method.

In eqs. (10) and (11), we use c to denote the structural phase speed and c' for the dynamic phase speed. However, we do not make this distinction hereafter unless the context is ambiguous.

When a large number of real or virtual sources are available, phase speeds at $\boldsymbol{r}$ can be binned by the azimuth of propagation. The mean and standard deviation of the mean (SDOM) in each bin are then computed (Lin et al., 2009), producing results such as those in **Fig. 5** for the 30 s Rayleigh wave at four locations based on the different methods we consider here. We then apply a least-squares fit (e.g. Tarantola, 2005) to the binned statistics, assuming that the dependence of phase speed on the azimuth (clockwise from north), ψ, is approximated by weak 2ψ anisotropy (e.g. Smith and Dahlen, 1973) and possible apparent 1ψ anisotropy (e.g. Lin and Ritzwoller, 2011a):

$$c(\psi) = \bar{c}\left(1 + \frac{A_1}{2}\cos(\psi - \psi_1) + \frac{A_2}{2}\cos 2(\psi - \psi_2)\right). \tag{12}$$

Here, $\bar{c}$ is the isotropic phase speed with the "bar" denoting an average over azimuth. The anisotropic parameters are (A_1, ψ_1), which represent the peak-to-peak relative amplitude and the fast direction of the 1ψ component, and (A_2, ψ_2), which are the peak-to-peak relative amplitude and the fast direction of the 2ψ component. We estimate associated uncertainties in each of the estimated quantities by standard error propagation, which we denote as $\sigma_{\bar{c}}, \sigma_{A_1}, \sigma_{\psi_1}, \sigma_{A_2}$, and σ_{ψ_2}.

In practice, we perform tomography on a $0.2° \times 0.2°$ spatial grid. From 10 s period to 40 s period we apply eikonal tomography to results from the ambient noise methods $\mathcal{I}_2^{AN}$, ${}^{ell}\mathcal{I}_3^{DW}$ and ${}^{hyp}\mathcal{I}_3^{DW}$, and from 28 s period to 80 s period we use Helmholtz tomography on the earthquake data. Thus, the phase speed maps from ambient noise data and earthquake data overlap from 28 s to 40 s period. We compute isotropic phase speeds, $\bar{c}$, on this grid, which results in a resolution equal to about the average station spacing (∼70 km) (Lin et al., 2009). However, to estimate azimuthal anisotropy, phase speeds from each point on the $0.2° \times 0.2°$ grid are combined with those from the eight neighbors to produce results on a $0.6° \times 0.6°$ grid, which lowers the resolution to ∼1.2° or 130 km.

The complementarity and consistency between the different data types can be visualized in the local anisotropy observations. **Fig. 5** shows measurements of the azimuthal distribution of phase speed for the 30 s Rayleigh wave at several locations. For example, near the Juan de Fuca Ridge (**Fig. 5(first row)**), ambient noise-based data (**Figs 5aei**) have azimuthal gaps for azimuths $\psi > 180°$ because of the lack of stations toward the west, while earthquake data (**Fig. 5m**) provide complementary azimuths using earthquakes from the west (**Fig. 1b**). Moreover, ambient noise-based data generally have larger uncertainties from the west than from the east (**Figs 5a-l**) because OBS measurements tend to have lower signal-to-noise ratios than land stations, while earthquake data have smaller uncertainties from the west (**Figs 5m-p**) because more earthquakes lie west of our study area (**Fig. 1b**). Thus, the composite data (**Figs 5q-t**) provide better azimuthal coverage than each data type alone. Estimates of 2ψ anisotropy fast directions, ψ_2, from the different methods mostly differ by $< 15°$ ($< 10\%$ fractional uncertainty for the azimuthal range of $180°$) while the amplitude of 2ψ anisotropy, A_2, can differ by $> 1\%$ ($> 30\%$ fractional uncertainty for an amplitude of 3%).

To compare results from pairs of different methods, we use Welch's unequal variances t-test. Assume we are comparing results from two methods denoted α and β, where α and β can take the values $\mathcal{I}_2^{AN}$, ${}^{hyp}\mathcal{I}_3^{DW}$, ${}^{ell}\mathcal{I}_3^{DW}$, and EQ for two-station interferometry ($\mathcal{I}_2^{AN}$), three-station interferometry (${}^{hyp}\mathcal{I}_3^{DW}$or ${}^{ell}\mathcal{I}_3^{DW}$), and earthquake tomography (EQ). Consider two isotropic phase speed maps computed with any two methods α and β, $\bar{c}_\alpha(\boldsymbol{r})$ and $\bar{c}_\beta(\boldsymbol{r})$, with associated uncertainty maps, $\sigma_{\bar{c}_\alpha}(\boldsymbol{r})$ and $\sigma_{\bar{c}_\beta}(\boldsymbol{r})$ at position $\boldsymbol{r}$. We then compute the following comparison statistics for the phase speeds:

$$\epsilon_{\bar{c};\alpha\beta}(\boldsymbol{r}) \equiv \sqrt{\sigma^2_{\bar{c}_\alpha}(\boldsymbol{r}) + \sigma^2_{\bar{c}_\beta}(\boldsymbol{r})}, \tag{13}$$

$$\Delta_{\bar{c};\alpha\beta}(\boldsymbol{r}) \equiv \frac{\bar{c}_\alpha(\boldsymbol{r}) - \bar{c}_\beta(\boldsymbol{r})}{\epsilon_{\bar{c};\alpha\beta}(\boldsymbol{r})}, \tag{14}$$

at location $\boldsymbol{r}$. $\epsilon_{\bar{c};\alpha\beta}(\boldsymbol{r})$ denotes the "combined phase speed uncertainty map" from methods α and β. $\Delta_{\bar{c};\alpha\beta}(\boldsymbol{r})$ is the "normalized phase speed difference map" between methods α and β. $\Delta_{\bar{c};\alpha\beta}(\boldsymbol{r})$ is unitless but $\epsilon_{\bar{c};\alpha\beta}(\boldsymbol{r})$ has the same unit as $\sigma_{\bar{c}}$ (m/s).

For all pairs of maps, we also compute analogues to eqs. (13) and (14) for the anisotropic quantities A_2 and ψ_2: Δ_{A_2}, Δ_{ψ_2}, ϵ_{A_2}, and ϵ_{ψ_2}. Carrying along the subscripts in Δ and ϵ is cumbersome, so we suppress them wherever context can determine their values. In all cases, Δ is unitless, but ϵ_{A_2} has the same unit as A_2 (%) and ϵ_{ψ_2} has the same unit as ψ_2 (°).

For a quantity x (e.g. Δ, ϵ), we use $\langle x \rangle$ to denote its spatial mean and $\langle x^2 \rangle$ to denote its spatial standard deviation. For example, the spatial mean and standard deviation of the normalized difference between two maps, Δ, are as follows:

$$\langle \Delta \rangle \equiv \frac{1}{M} \sum_{i=1}^{M} \Delta(\boldsymbol{r}_i), \tag{15}$$

$$\langle \Delta^2 \rangle \equiv \left(\frac{1}{M} \sum_{i=1}^{M} (\Delta(\boldsymbol{r}_i) - \langle \Delta \rangle)^2 \right)^{\frac{1}{2}}, \tag{16}$$

where Δ is defined at M spatial grid locations.

$\langle \Delta \rangle$ signifies the level of systematic bias in the quantity presented on the two maps. For two maps not to be considered systematically different, $|\langle \Delta \rangle| < 1$; that is, the spatial mean of the difference is less than the average uncertainty. $\langle \epsilon \rangle$ indicates the spatially averaged uncertainty in a quantity for the two maps. Multiplying $\langle \Delta \rangle$ by $\langle \epsilon \rangle$ gives an approximate estimate of systematic bias specified with units. Also, $\langle \Delta^2 \rangle$ signifies the standard deviation of the normalized difference taken over the maps. If we have estimated the uncertainties reliably then $\langle \Delta^2 \rangle \sim 1$. If $\langle \Delta^2 \rangle > 1$, then we may have underestimated the uncertainties in one or the other or both of the maps under comparison.

4.2 Isotropic phase speed maps

Examples of the estimated phase speed maps, $\bar{c}(\boldsymbol{r})$, and uncertainties, $\sigma_{\bar{c}}(\boldsymbol{r})$, produced with the different methods are shown in **Fig. 6** for 30 s period. The maps are qualitatively similar to one another, with higher phase speeds in the oceanic regions (due to thinner crust) and more variable phase speeds on land. Several normalized difference maps, $\Delta_{\bar{c}}$, at 30 s period are displayed in **Fig. 7**. The patterns of the differences are relatively random (**Figs 7aceg**), except the systematic differences near the Cascade Range between the $\mathcal{I}_2^{AN}$map and the earthquake map (**Fig 7e**). This stripe where earthquake derived phase speeds are faster than those from ambient noise has been noted before (e.g. Yang and Ritzwoller, 2008), but the discrepancy reduces as the number of earthquakes increases (e.g. Shen and Ritzwoller, 2016). Right to the west of this stripe is one smaller in area and magnitude where earthquake derived phase speeds are slower than those from ambient noise. The cause of the discrepancy remains poorly understood (e.g. Kästle et al., 2016).

Statistics describing the different maps are plotted in each panel of the bottom row of **Fig. 7**. For example, in the comparison between $\mathcal{I}_2^{AN}$and ${}^{hyp}\mathcal{I}_3^{DW}$(**Figs 7cd**), $\langle \Delta \rangle = 0.6$, $\langle \Delta^2 \rangle = 1.9$, and $\langle \epsilon \rangle = 13$ m/s. That is, the spatial average of the normalized difference in phase speed between these methods is 0.6, which means that $\mathcal{I}_2^{AN}$produces faster phase speeds at this period than ${}^{hyp}\mathcal{I}_3^{DW}$by a little more than half of the average uncertainty level, which is 13 m/s. This is below the threshold, $|\langle \Delta \rangle| > 1$, for the maps to be considered systematically different. The standard deviation of the normalized difference taken over the maps, however, is 1.9. This indicates that our uncertainties for either or both of $\mathcal{I}_2^{AN}$ and ${}^{hyp}\mathcal{I}_3^{DW}$ are probably underestimated. Other comparisons presented in **Fig. 7** are similar: systematic bias between the maps is below the threshold that we use to indicate the maps are significantly different but our uncertainties tend to be underestimated. Multiplying uncertainties by $\sim$2 would be needed to rectify this at this period.

We perform similar analyses across all periods where the results of the methods overlap, and the statistics are summarized in **Fig. 8** in which we plot the spatial mean $\langle\Delta\rangle$ and standard deviation $\langle\Delta^2\rangle$ of the normalized differences of each pair of phase speed maps along with the mean of the combined uncertainties $\langle\epsilon\rangle$.

The results relevant to an assessment of systematic bias between pairs of maps, which are the basis for the combination of the data from the different methods, are shown in **Fig. 8 (first row)**. The normalized bias, $\langle\Delta\rangle$, between the maps typically lies between ±1. The primary exception is the comparison between the ${}^{ell}\mathcal{I}_3^{DW}$ and ${}^{hyp}\mathcal{I}_3^{DW}$ methods in the narrow band between 14 and 18 s. From the general low level of systematic bias between the methods, we conclude that the maps from the different methods are consistent and, therefore, the measurements that derive from the methods can be combined.

One can approximately convert the systematic bias results in **Fig. 8 (first row)** from unitless to units of m/s, by multiplying by the spatially averaged combined uncertainties, $\langle\epsilon\rangle$, presented in **Fig. 8 (third row)**. These uncertainties minimize near 20 s period ($\langle\epsilon\rangle \sim 10$ m/s) and increase at shorter and longer periods ($\langle\epsilon\rangle \sim 20$ m/s), which is consistent with the quality of the dispersion measurements (**Fig. 4**). An average value of bias is about $\langle\Delta\rangle = 0.5$, which when multiplied by an average value of $\langle\epsilon\rangle \sim 14$ m/s, converts to $\sim$7 m/s ($\sim$0.2% for a phase speed of 3.5 km/s), which is appropriately low.

The standard deviations of the normalized differences between the maps, $\langle\Delta^2\rangle$, which are the basis for the assessment of the adequacy of the uncertainty estimates, are shown in **Figs 8 (second row)**. The values generally are greater than 1.0, lying between 1.5 and 3. Thus, uncertainty estimates may be too small by between 50% to 200%. However, some of these differences may not come from random errors because there are various degrees of differences between different pairs of methods. For example, ${}^{ell}\mathcal{I}_3^{DW}$ is systematically slower than $\mathcal{I}_2^{AN}$ at shorter periods ($\langle\Delta\rangle \geq 0.5$ between 14 s and 26 s, **Fig. 8a**), which may call into question the straight-ray correction and further improvements might require use of finite frequency sensitivity kernels. In addition, $\langle\Delta^2\rangle$ generally increases with period, indicating the increasing finite frequency effects, which are not considered in eikonal tomography (e.g. Lin and Ritzwoller, 2011b). Also, agreement between $\mathcal{I}_2^{AN}$ and the three-station methods ($1.5 \leq \langle\Delta^2\rangle \leq 2.5$, **Figs 8ac**) is slightly better than that between $\mathcal{I}_2^{AN}$ and earthquake results ($2.5 \leq \langle\Delta^2\rangle \leq 3$, **Fig. 8e**), which is expected because three-station methods are based on and thus correlated with $\mathcal{I}_2^{AN}$ (Sheng et al., 2018).

In summary, to produce $\langle\Delta^2\rangle \sim 1$ requires the uncertainties $\sigma_{\bar{c}}$ to be upscaled by a factor of about 2 on average. Some of this upscaling will encompass the observed systematic biases between the maps. But, such biases are small enough for us to conclude that for isotropic phase speed, measurements from the different methods can be combined consistently into a single data set (**section 5.1**).

4.3 Azimuthally anisotropic phase speed maps

4.3.1 Observation of apparent 1ψ anisotropy

Observations of apparent Rayleigh wave 1ψ azimuthal anisotropy (360° periodicity) have been reported in the western U.S. (Lin and Ritzwoller, 2011b) and Alaska (Feng and Ritzwoller, 2020), which are largely attributed to backward scattering from strong lateral isotropic velocity contrasts (Lin and Ritzwoller, 2011a). Because 1ψ anisotropy violates reciprocity and thus is non-physical, we attempt to detect it and to remove the bias it may cause in both isotropic and 2ψ anisotropic phase speed estimates (**Fig. 9**). In fact, by fitting local azimuth-dependent phase speeds with eq. (12), we do observe strong 1ψ anisotropy ($> 3\%$) at long periods (> 50 s), especially around the Cascade Range (**Figs 9ce**). The fast directions of 1ψ anisotropy, ψ_1, mostly point towards the faster isotropic phase speed (**Figs 9df**), consistent with their being caused by backward scattering. Compared with fitting 2ψ anisotropy only, fitting 1ψ and 2ψ anisotropy simultaneously makes a difference in 2ψ fast directions (MAD (median absolute deviation) of the difference $\sim$10° (with respect to 0°)) and in isotropic phase speeds (MAD of the difference $\sim$11 m/s).

4.3.2 Comparison of anisotropic maps from different methods

An example of 2ψ anisotropy (fast directions, ψ_2, and amplitudes, A_2) with associated uncertainty estimates (σ_{ψ_2} and σ_{A_2}) constructed with the different methods is shown in **Fig. 10** at 30 s period. Qualitatively, the patterns of fast directions, amplitudes, and uncertainties between the methods are similar to one another, such as the two stripes of relatively strong anisotropy near the Cascade Range and at old lithospheric ages on the oceanic plate.

A quantitative comparison of the maps at 30 s period is presented in **Fig. 11**, which displays Δ_{ψ_2} and Δ_{A_2} between the method $\mathcal{I}_2^{AN}$ and other methods. For fast directions ψ_2, relatively large differences are principally observed where at least one of the methods yields low amplitudes, A_2, or near the periphery of the maps where azimuthal coverage for the noise-based methods is poor (**Figs 11aei**). Differences in A_2 appear to be more random although somewhat correlated with those in ψ_2 (**Figs 11cgk**).

Spatial statistics are summarized via histograms of the normalized differences for fast directions ψ_2 (**Figs 11bfj**) and amplitudes A_2 (**Figs 11dhl**). For instance, statistics for the comparison of A_2 between $\mathcal{I}_2^{AN}$ and ${}^{ell}\mathcal{I}_3^{DW}$ are: $\langle\Delta_{A_2}\rangle = -0.2$, $\langle\Delta^2_{A_2}\rangle = 2.4$, and

$\langle\epsilon_{A_2}\rangle = 0.36\%$ (**Fig. 11d**). That is, the spatial average of the normalized difference in anisotropy amplitude between the methods is -0.2, which means that $\mathcal{I}_2^{AN}$ produces lower anisotropy amplitudes at this period than ${}^{ell}\mathcal{I}_3^{DW}$ by about one fifth of the average uncertainty, which is 0.36%. This is compatible with the criterion, $|\langle\Delta_{A_2}\rangle| \leq 1$, for the maps not to be considered systematically different. As indicated by $\langle\Delta^2_{A_2}\rangle = 2.4$, our uncertainties are probably underestimated for either or both of the methods. Other comparisons presented in **Fig. 11** are similar: systematic bias between the maps is below the threshold for indicating the maps to be systematically different while the uncertainties tend to be underestimated by about a factor of two.

Similar analyses are performed across all periods where results from the different methods overlap, and the statistics are plotted versus period for both anisotropy amplitudes and fast directions in **Fig. 12**.

The assessment of systematic bias between different methods are shown in **Fig. 12** for anisotropy amplitudes (**Fig. 12djpv**) and fast directions (**Fig. 12agms**). In general, the level of systematic bias between the methods is low ($|\langle\Delta\rangle| < 1$), except between $\mathcal{I}_2^{AN}$ and EQ at periods of 36–40 s where amplitudes from EQ are smaller than $\mathcal{I}_2^{AN}$. Thus, we conclude that the maps from the different methods are compatible, and the measurements derived from the methods can be combined.

The systematic bias can be converted from dimensionless to units if multiplied by the mean uncertainties. These uncertainties minimize around 24 s ($\langle\epsilon_{\psi_2}\rangle \sim 7°$ and $\langle\epsilon_{A_2}\rangle \sim 0.3\%$) and increase at shorter and longer periods ($\langle\epsilon_{\psi_2}\rangle \sim 10°$ and $\langle\epsilon_{A_2}\rangle \sim 0.6\%$). When multiplied by average uncertainties of $\langle\epsilon_{\psi_2}\rangle \sim 9°$ and $\langle\epsilon_{A_2}\rangle \sim 0.4\%$, an average value of bias of $\sim$0.5 corresponds to $\sim$5° for ψ_2 and $\sim$0.2% for A_2, which are relatively low.

The underestimation of uncertainties for anisotropic parameters is comparable to that for isotropic phase speed. The standard deviations of the normalized differences, $\langle\Delta^2_{\psi_2}\rangle$ and $\langle\Delta^2_{A_2}\rangle$, are all greater than one, mostly between 1.5 and 2.5, for both ψ_2 (**Figs 12bhnt**) and A_2 (**Figs 12flrx**). In addition, $\langle\Delta^2_{\psi_2}\rangle$ and $\langle\Delta^2_{A_2}\rangle$ also increase with period in general. These values are consistent with $\langle\Delta^2_{\bar{c}}\rangle$ (**Fig. 8**) and thus will be reduced to a similar level if uncertainties for azimuthally binned phase speed measurements are appropriately upscaled before fitting (**section 4.1**).

In summary, to yield $\langle\Delta^2_{\psi_2}\rangle$ and $\langle\Delta^2_{A_2}\rangle$ about unity indicates that the uncertainties, σ_{ψ_2} and σ_{A_2}, need to be upscaled by a factor of $\sim$2, which is consistent with the extent of underestimation for isotropic phase speed uncertainties $\sigma_{\bar{c}}$ (**section 4.2**). Thus, an appropriate upscaling of uncertainties before fitting the azimuthally binned phase speeds (**section 4.1**) will reduce $\langle\Delta^2_{\bar{c}}\rangle$, $\langle\Delta^2_{\psi_2}\rangle$ and $\langle\Delta^2_{A_2}\rangle$ all to a similar level ($\sim$1). This upscaling will also reduce the amplitude of the normalized systematic bias $|\langle\Delta\rangle|$ between the methods, so that an average bias about half the uncertainty level will be reduced to only a quarter of the upscaled uncertainty. Such small biases are compatible with the hypothesis that the methods are not systematically different, and thus we combine measurements from different methods to produce a single composite result (**section 5.2**).

5 Composite results

To construct composite results, we combine the source-specific phase speed measurements across all methods (**Fig. 5**). Compared with combining the phase speed maps across methods (**Fig. 6**), combining the source-specific measurements before binning and stacking has the advantage of utilizing the complementary azimuthal coverages between the methods. Specifically, to construct a composite result with uncertainty at a given period and location, the source-specific phase speed measurements from all methods that exist at the location and period are combined by computing their mean and the SDOM for each azimuthal bin as observations (**Fig. 5e**). Then we fit eq. (12) to the binned statistics over azimuth to estimate the isotropic and anisotropic parameters with associated uncertainties (**section 4.1**). We repeat this process at all locations across the region of study to produce the isotropic and anisotropic maps at the period.

5.1 Composite isotropic phase speed maps

In general, phase speeds on the oceanic plates are faster than the continental shelf and continents, and also vary less with period (**Fig. 13**). Near the contineta shelf, phase speeds are relatively low, delineating the dichotomy between onshore and offshore structures. On the continents, phase speeds are more variable spatially and across different periods.

Previous studies have already constructed isotropic maps onshore (e.g. Lin et al., 2008; Shen and Ritzwoller, 2016), which are generally consistent with our results there. Less work has been done offshore, and our discussion of the composite maps here will focus on the offshore and near coastal regions for this reason (**Fig. 13**).

At 10 s period (**Figs 13ab**), the results derive from the two- and three-station ambient noise methods alone. Rayleigh wave phase speed at this period is mostly sensitive to oceanic uppermost mantle and continental crustal structures. The phase speed at this period in the oceanic plate is much faster (> 3.6 km/s) than in the continent ($\sim$3.1 km/s). The Juan de Fuca Ridge, the Blanco Transform Fault, and the Gorda Ridge are delineated as relative slow anomalies offshore. A prominent slow stripe (< 2.8 km/s) along the continental shelf (especially to the west of Washington) clearly separates the land from the ocean and may derive from elevated fluid content in the crust. Uncertainties $\sigma_{\bar{c}}$ on the continents are quite small ($\sim$5 m/s), while the $\sigma_{\bar{c}}$ offshore is substantially larger ($\sim$10 m/s), especially on the continental shelf ($\sim$15 m/s).

At 20 s period (**Figs 13cd**), the results are also derived exclusively from the ambient noise methods. Rayleigh waves at this period are largely sensitive to the uppermost mantle offshore, and the middle and lower crust onshore with some sensitivity to the mantle in areas of relatively thin continental crust. The Cobb Hotspot near the Juan de Fuca Ridge stands out as a relatively slow anomaly in the ocean. The slow anomalies along the coast march landward compared to their location at 10 s period (**Fig. 13a**) and apparently break into two distinct zones in the northern and southern continental margin. Uncertainties $\sigma_{\bar{c}}$ are much smaller than at 10 s period ($\sim$3 m/s onshore and $\sim$5 m/s offshore) because of the increase in SNR at 20 s period and the corresponding increase in the number of measurements (**section 3**).

At 30 s period (**Figs 13ef**), results are from both earthquakes and ambient noise. The Rayleigh wave at this period is largely sensitive to the uppermost mantle offshore, and the lower crust, crustal thickness, and uppermost mantle onshore. The slow anomalies along the continental margin again break into northern and southern regions, but have lower amplitudes compared to shorter periods (**Figs 13ac**). Uncertainties $\sigma_{\bar{c}}$ are relatively homogeneous ($\sim$5 m/s) and are smaller than those from the individual data sets (**Fig. 6**) because of the increase of the number of measurements.

At 60 s period (**Figs 13gh**), the map is from earthquake data alone and Rayleigh wave dispersion is mainly sensitive to the upper mantle across the entire region. The two slow patches on the northern and southern continental margin are still clearly depicted but move oceanward again compared to 30 s period. Uncertainties $\sigma_{\bar{c}}$ have increased relative to 30 s period, both onshore ($\sim$7 m/s) and particularly offshore ($\sim$15 m/s).

5.2 Composite anisotropic maps

Generally, anisotropy amplitudes A_2 increase with lithospheric age on the oceanic plates and decrease with period (**Fig. 16**). A_2 is relatively weak ($< 2\%$) on the continental shelf in general. On the continent, A_2 near the Cascade Range is relatively strong across most periods. In addition, fast directions ψ_2 are ridge-perpendicular at young ages and rotate counterclockwise with increasing age in general, although variations exist between different periods and between the Juan de Fuca and Gorda Plates. Near the continental shelf, ψ_2 is more variable and shows both trench-perpendicular and trench-parallel directions at different locations and periods. On the continent, ψ_2 varies with location and period in a complex manner.

Because anisotropic structures onshore have been well studied and our results do not substantially differ from previous studies (e.g. Lin et al., 2011; Lin and Ritzwoller, 2011b), the following discussion of the composite anisotropic maps focuses on the offshore and near the coastal regions (**Fig. 16**).

At 12 s period (**Figs 16a-c**), maps are constructed from data using a combination of the ambient noise methods $\mathcal{I}_2^{AN}$, ${}^{ell}\mathcal{I}_3^{DW}$ and ${}^{hyp}\mathcal{I}_3^{DW}$. On the Juan de Fuca Plate, 2ψ fast directions ψ_2 rotate slightly counterclockwise from ridge-perpendicular to W-E as the plate ages, which is consistent with the paleo-spreading directions (calculated from gradients of lithospheric age (Wilson, 1993)). The anisotropy amplitudes A_2 generally increase with age. Near the Blanco Transform, fast axes ψ_2 run predominantly W-E, counterclockwise from the fault strike. On the Gorda Plate, fast axes rotate clockwise from ridge-perpendicular as the plate ages, aligning approximately with paleo-spreading directions, and A_2 is strong ($> 3\%$) except near the Gorda Ridge. On the northern continental shelf, fast axes run NW-SE and strong A_2 is observed. Relatively large uncertainties in ψ_2 are mainly due to small amplitudes, A_2 (**Fig. 16b**), while large uncertainties in A_2 are mostly on the continental shelf due to low data quality (**Fig. 16c**). At this period, the Rayleigh wave is mainly sensitive to the oceanic uppermost mantle, so azimuthal anisotropy from Rayleigh waves is somewhat comparable to that from P_n waves. Indeed, the following patterns are also observed in 2ψ fast directions from P_n (VanderBeek and Toomey, 2017; VanderBeek and Toomey, 2019): ridge-perpendicular near the Juan de Fuca Ridge, W-E on the Juan de Fuca Plate interior and near the Blanco Transform, and clockwise rotation with age on the Gorda Plate.

At 30 s period (**Figs 16d-f**), the results combine ambient noise and earthquake data. On the Juan de Fuca Plate, fast axes ψ_2 are generally consistent with paleo-spreading directions except at the older ages (> 7 Ma) where they rotate counterclockwise from W-E towards SW-NE to align apparently with absolute plate motion directions. A high amplitude A_2 stripe is also observed at these older ages along the trench. On the Gorda Plate, fast axes are predominantly oriented W-E, apparently counterclockwise from paleo-spreading directions. On the continental shelf, fast axes show a substantial trench-parallel component and are substantially different from those on the oceanic plate as well as on the continent.

At 50 s period (**Figs 16g-i**), the results are from earthquake data alone. Near the Blanco Transform, fast axes ψ_2 align well with the strike of the fault, which is different from the shorter periods (**Figs 16a-f**). Along the trench on the oceanic plates, the strong A_2 stripe appears to diminish. On the continental shelf, fast axes are predominantly trench-perpendicular while the amplitudes A_2 are relatively weak ($< 1\%$).

At 80 s period (**Figs 16j-l**), results also are only from earthquake data. Near the Blanco Transform, strong amplitudes A_2 are observed and fast axes ψ_2 are parallel to the fault strike. On the Juan de Fuca Plate, the strong A_2 stripe along the trench apparent at shorter periods has disappeared. On the Gorda Plate, fast axes rotate counterclockwise from ridge-perpendicular to W-E as the plate ages, and amplitudes A_2 are strong ($> 3\%$) except near the Gorda Ridge.

Crustal and mantle anisotropy near a target location is reflected in anisotropic dispersion curves, which are constructed by extracting the anisotropic parameters A_2 and ψ_2 from the period-dependent maps (e.g. Lin et al., 2011). The period-dependent patterns of fast axes and amplitudes differ appreciably at different locations, as **Fig. 17** shows for four locations. At a point near the Juan de Fuca Ridge, a change in fast axis ψ_2 from ridge-perpendicular (NW-SE) to nearly N-S corresponds to the minimum of amplitude A_2 (**Figs 17ab**), suggesting a change of anisotropy at deeper depth. For a point within the Juan de Fuca Plate, ψ_2 is mostly W-E while A_2 slightly increases then decreases with period (**Figs 17cd**), suggesting vertically relatively coherent deformation.

At a point on the continental shelf, ψ_2 is predominantly trench parallel (NE-SW) and A_2 varies slowly with period (**Figs 17ef**), indicating complicated changes in anisotropy between the sediments and crust. For a point in Oregon, both ψ_2 and A_2 apparently break into three segments with ψ_2 rotating counterclockwise from N-S to W-E then to NE-SW and A_2 increasing then decreasing with period (**Figs 17gh**), indicating distinctions between upper crust, lower crust, and mantle. Such anisotropic dispersion curves can serve as the basis for 3-D azimuthally anisotropic model inversions (e.g. Lin et al., 2011; Feng and Ritzwoller, 2020). When information about radial anisotropy is available from Love wave dispersion (e.g. Moschetti et al., 2010; Feng and Ritzwoller, 2019), azimuthally and radially anisotropic dispersion curves can be combined to constrain a tilted depth-dependent hexagonally symmetric medium for simultaneous explanation of azimuthal and radial anisotropy (e.g. Xie et al., 2015; Xie et al., 2017). Anisotropy from surface waves can also complement body wave observations, such as shear wave splitting (e.g. Martin-Short et al., 2015; Bodmer et al., 2015) and P_n waves (e.g. VanderBeek and Toomey, 2017; VanderBeek and Toomey, 2019), to achieve a better depth resolution (e.g. Lin et al., 2011; Eilon and Forsyth, 2020).

6 Comparison with a previous study

Janiszewski et al. (2019) constructed Rayleigh wave isotropic phase speed maps from two-station ambient noise interferometry ($\mathcal{I}_2^{AN}$) and earthquake tomography. We compare both our local dispersion curves and phase speed maps with theirs and find significant discrepancies. We do not completely understand the cause of the discrepancies, but an appreciable part probably results from differences in methodology between our study and theirs.

Dispersion curves at a location extracted from the phase speed maps at different periods should be reasonably smooth to make physical sense. For visual comparison, **Fig. 14** presents dispersion curves at several locations from our different methods and from Janiszewski et al. (2019). The dispersion curves from our methods are presented as corridors with a thickness defined by our uncertainties at the location: $\bar{c} \pm 2\sigma_{\bar{c}}$. Our results nearly overlap each other, which illustrates the consistency that emerges from our different methods. The fact that Janiszewski et al. (2019) also estimated uncertainties allows us to present their results at the same locations similarly. We find, however, that significant discrepancies ($> 5\%$) appear between our results and those of Janiszewski et al. (2019), even on the continent (**Fig. 14d**).

A more detailed comparison of our phase speed maps with those from Janiszewski et al. (2019) is presented here in terms of maps and histograms of raw differences. We do not use normalized differences as in **section 4.1**, because their approach to uncertainty estimates is different from ours. We present comparisons at each period in the supplementary material (**Figs S1-S8**). The spatial mean of the raw differences and the combined uncertainties are summarized in **Fig. 15**.

Our maps are systematically faster than their ambient noise maps, and the bias increases with period from ∼15 m/s at 10 s to ∼60 m/s at 20 s, which corresponds to ∼0.5% and ∼2% for a phase speed of 3 km/s, respectively. This discrepancy may be due to the fact that they did not denoise the OBS data with tilt and compliance noise corrections (their two-station interferograms are from Gao and Shen (2015)). In contrast, our maps are systematically slower than their earthquake maps, and the bias also increases with period but with an opposite sign from −20 m/s at 20 s to −40 m/s at 80 s (∼1% for a phase speed of 3 km/s), which might be due to different implementations of Helmholtz tomography (Jin and Gaherty, 2015). The largest bias is between their ambient noise and earthquake results (earthquake results ∼70 m/s faster), which they attribute partly to the difference in station distribution.

7 Conclusion

Our final product is a set of composite Rayleigh wave isotropic and azimuthally anisotropic phase speed maps from 10 s to 80 s period, constructed by combining earthquake (28–80 s) and ambient noise-based (10–40 s) data. Compared with two-station interferometry ($\mathcal{I}_2^{AN}$), three-station direct-wave interferometry methods (${}^{ell}\mathcal{I}_3^{DW}$ and ${}^{hyp}\mathcal{I}_3^{DW}$) provide $> 50\%$ enhancement in the SNR and the number of dispersion measurements which is particularly noteworthy in the noisier oceanic environment (**section 3**). This illustrates the potential utility of the method in other amphibious settings such as off Alaska using data from AACSE (Alaska Amphibious Community Seismic Experiment, (Abers and Wiens, 2018)). The isotropic (**section 4.2**) and azimuthally anisotropic (**section 4.3**) phase speed maps based on earthquakes and ambient noise data agree within about twice the estimated uncertainties. This reflects positively on the effectiveness of denoising of OBS data (**section 2.1.1**) and on de-biasing the three-station methods (**section 2.1.2**). Compared with maps from each method alone, the composite maps reduce uncertainties, broaden the bandwidth, and improve azimuthal coverage (**section 5**).

The composite isotropic phase speed maps have a resolution ∼0.6° with mean fractional uncertainties of 0.1–0.3% onshore (4–8 m/s) and 0.15–0.5% offshore (5–20 m/s). Uncertainties minimize between 20 s and 40 s period and increase at shorter and longer periods. Our comparisons between different methods indicate that we underestimate uncertainties by 50–150%. Isotropic anomalies (**section 5.1**) qualitatively correlate with known geological features, such as the Juan de Fuca and Gorda Ridges, the Cobb hotspot, the Blanco Transform Fault, and the Cascade Range.

The composite azimuthally anisotropic phase speed maps have a resolution of ∼1.2° with mean fractional uncertainties of 1–5% onshore (2–10°) and 2–6% offshore (3–12°) for fast direction, ψ_2, and 6–30% onshore (0.1–0.2%) and 11–40% offshore (0.15–0.5%)

for amplitude, A_2. Uncertainties vary with period similarly to those of isotropic maps, and are similarly underestimated for true uncertainties (**section 4.3**). On the oceanic plate, the 2ψ fast directions qualitatively align with paleo-spreading directions while the 2ψ amplitudes generally increase with lithospheric age, both showing nontrivial variations with period (**section 5.2**). Strong ($> 3\%$) apparent 1ψ azimuthal anisotropy is observed at long periods (> 50 s) around the Cascade Range, probably caused by backward scattering from strong isotropic heterogeneity (**section 4.3.1**).

The composite phase speed maps are designed to serve as a basis for future work. One possible extension is to invert for 3-D shear velocity models based on the maps, potentially jointly with other observables such as receiver functions (e.g. Janiszewski and Abers, 2015; Audet, 2016; Rychert et al., 2018), Rayleigh wave ellipticity, and Rayleigh wave displacement to pressure ratios (e.g. Ruan et al., 2014). Different from traditional seismic parameterizations, thermal parameterizations (e.g. Shapiro and Ritzwoller, 2004) may be used as hypothesis tests on the thermal state of the oceanic lithosphere (e.g. Tian et al., 2013). Surface wave azimuthal anisotropy observations can complement body wave data such as shear wave splitting (e.g. Martin-Short et al., 2015; Bodmer et al., 2015) for 3-D anisotropic model inversions (e.g. Lin et al., 2011). Observations of Love waves can be combined with Rayleigh waves to constrain a tilted hexagonally symmetric medium for simultaneous explanation of azimuthal and radial anisotropy (e.g. Xie et al., 2015). Such anisotropic models may provide constraints for geodynamical simulations of deformation across and beneath the lithosphere.

Acknowledgement

We thank Helen Janiszewski for providing phase speed maps (Janiszewski et al., 2019) to compare with our own and Weisen Shen for sharing onshore ambient noise correlations and earthquake dispersion measurements from the TA (Shen and Ritzwoller, 2016). We are also grateful to Wei Mao, Anne Sheehan, Craig Jones, Fan-Chi Lin, and Victor Tsai for helpful discussions. The authors are grateful to the Cascadia Initiative Expedition Team for acquiring the Amphibious Array Ocean Bottom Seismograph data and appreciate the open data policy that makes these data available. This work utilized resources from the University of Colorado Boulder Research Computing Group, which is supported by the National Science Foundation (awards ACI-1532235 and ACI-1532236), the University of Colorado Boulder, and Colorado State University. **Author contributions:** S.Z. computed three-station interferograms, applied tomography analysis, and co-wrote the paper. H.W. preprocessed noise data and computed two-station interferograms. M.W. preprocessed and measured dispersion from earthquake data. M.H.R. designed and guided the project and co-wrote the paper. All authors discussed the results and provided comments on the manuscript. **Funding:** Aspects of this research were supported in part by NSF grants EAR-1537868, EAR-1645269, and EAR-1928395 at the

University of Colorado at Boulder. **Data and materials availability:** Our composite phase speed maps are available on Zenodo (doi: 10.5281/zenodo.3973769). Source codes for this project are available on GitHub (`https://github.com/NoiseCIEI`) or upon request from the corresponding author. The offshore data used in this research were provided by instruments from the Ocean Bottom Seismograph Instrument Pool (`http://www.obsip.org`) which is funded by the National Science Foundation. OBSIP data are archived at the IRIS Data Management Center (`http://www.iris.edu`). The facilities of IRIS Data Services, and specifically the IRIS Data Management Center, were used for access to waveforms, related metadata, and/or derived products used in this study. IRIS Data Services are funded through the Seismological Facilities for the Advancement of Geoscience and EarthScope (SAGE) Proposal of the National Science Foundation under Cooperative Agreement EAR-1261681.

References

Abers, G. and D. Wiens (2018). "AACSE: Alaska Amphibious Community Seismic Experiment". International Federation of Digital Seismograph Networks. DOI: 10.7914/SN/XO_2018.

Atwater, B. F. (1987). "Evidence for great Holocene earthquakes along the outer coast of Washington State". *Science* 236.4804, pp. 942–944. DOI: 10.1126/science.236.4804.942.

Audet, P. (2016). "Receiver functions using OBS data: promises and limitations from numerical modelling and examples from the Cascadia Initiative". *Geophysical journal international* 205.3, pp. 1740–1755. DOI: 10.1093/gji/ggw111.

Barmin, M. P., M. H. Ritzwoller, and A. L. Levshin (2001). "A fast and reliable method for surface wave tomography". *Pure and applied geophysics* 158.8, pp. 1351–1375. DOI: 10.1007/978-3-0348-8264-4_3.

Bell, S., D. W. Forsyth, and Y. Ruan (2015). "Removing noise from the vertical component records of ocean-bottom seismometers: results from year one of the Cascadia Initiative". *Bulletin of the seismological society of america* 105.1, pp. 300–313. DOI: 10.1785/0120140054.

Bell, S., Y. Ruan, and D. W. Forsyth (2016). "Ridge asymmetry and deep aqueous alteration at the trench observed from Rayleigh wave tomography of the Juan de Fuca plate". *Journal of geophysical research: solid earth* 121.10, pp. 7298–7321. DOI: 10.1002/2016JB012990.

Bensen, G. D., M. H. Ritzwoller, M. P. Barmin, A. L. Levshin, F. Lin, M. P. Moschetti, N. M. Shapiro, and Y. Yang (2007). "Processing seismic ambient noise data to obtain reliable broad-band surface wave dispersion measurements". *Geophysical journal international* 169.3, pp. 1239–1260. DOI: 10.1111/j.1365-246X.2007.03374.x.

Bird, P. (2003). "An updated digital model of plate boundaries". *Geochemistry, geophysics, geosystems* 4.3. DOI: 10.1029/2001GC000252.

Bodmer, M., D. R. Toomey, E. E. Hooft, J. Nábělek, and J. Braunmiller (2015). "Seismic anisotropy beneath the Juan de Fuca plate system: Evidence for heterogeneous mantle flow". *Geology* 43.12, pp. 1095–1098. DOI: 10.1130/G37181.1.

Bodmer, M., D. R. Toomey, E. E. E. Hooft, and B. Schmandt (2018). "Buoyant asthenosphere beneath Cascadia influences megathrust segmentation". *Geophysical research letters* 45.14, pp. 6954–6962. DOI: 10.1029/2018GL078700.

Byrnes, J. S., D. R. Toomey, E. E. E. Hooft, J. Nábělek, and J. Braunmiller (2017). "Mantle dynamics beneath the discrete and diffuse plate boundaries of the Juan de Fuca plate: results from Cascadia Initiative body wave tomography". *Geochemistry, geophysics, geosystems* 18.8, pp. 2906–2929. DOI: 10.1002/2017GC006980.

Campillo, M. and A. Paul (2003). "Long-range correlations in the diffuse seismic coda". *Science* 299.5606, pp. 547–549. DOI: 10.1126/science.1078551.

Crawford, W. C. and S. C. Webb (2000). "Identifying and removing tilt noise from low-frequency (< 0.1 Hz) seafloor vertical seismic data". *Bulletin of the seismological society of america* 90.4, pp. 952–963.

Curtis, A., Y. Behr, E. Entwistle, E. Galetti, J. Townend, and S. Bannister (2012). "The benefit of hindsight in observational science: Retrospective seismological observations". *Earth and planetary science letters* 345-348, pp. 212–220. DOI: 10.1016/j.epsl.2012.06.008.

Curtis, A. and D. Halliday (2010). "Source-receiver wave field interferometry". *Physical review e* 81.4, p. 046601. DOI: 10.1103/PhysRevE.81.046601.

Dziewonski, A., S. Bloch, and M. Landisman (1969). "A technique for the analysis of transient seismic signals". *Bulletin of the seismological society of america* 59.1, pp. 427–444.

Eilon, Z. C. and G. A. Abers (2017). "High seismic attenuation at a mid-ocean ridge reveals the distribution of deep melt". *Science advances* 3.5, e1602829. DOI: 10.1126/sciadv.1602829.

Eilon, Z. C. and D. W. Forsyth (2020). "Depth dependent azimuthal anisotropy beneath the Juan de Fuca Plate system". *Journal of geophysical research: solid earth* n/a.n/a, e2020JB019477. DOI: 10.1029/2020JB019477.

Feng, L. and M. H. Ritzwoller (2020). "Azimuthal anisotropy of the crust and uppermost mantle beneath Alaska". *Submitted*.

— (2019). "A 3-D shear velocity model of the crust and uppermost mantle beneath alaska including apparent radial anisotropy". *Journal of geophysical research: solid earth* 124.10, pp. 10468–10497. DOI: 10.1029/2019JB018122.

Fenneman, N. M. and D. W. Johnson (1946). *Physical divisions of the United States*. Reston, VA: US Geological Survey.

Gao, H. (2016). "Seismic velocity structure of the Juan de Fuca and Gorda Plates revealed by a joint inversion of ambient noise and regional earthquakes". *Geophysical research letters* 43.10, pp. 5194–5201. DOI: 10.1002/2016GL069381.

Gao, H. and Y. Shen (2015). "A preliminary full-wave ambient-noise tomography model spanning from the Juan de Fuca and Gorda spreading centers to the Cascadia volcanic arc". *Seismological research letters* 86.5, pp. 1253–1260. DOI: 10.1785/0220150103.

GEBCO Compilation Group (2019). "GEBCO 2019 grid". DOI: 10.5285/836f016a-33be-6ddc-e053-6c86abc0788e.

Goldfinger, C., C. H. Nelson, A. E. Morey, J. E. Johnson, J. R. Patton, E. B. Karabanov, J. Gutierrez-Pastor, A. T. Eriksson, E. Gracia, G. Dunhill, R. J. Enkin, A. Dallimore, and T. Vallier (2012). *Turbidite event history—Methods and implications for Holocene paleoseismicity of the Cascadia subduction zone*. USGS Numbered Series 1661-F. Reston, VA: U.S. Geological Survey. DOI: 10.3133/pp1661F.

Hawley, W. B. and R. M. Allen (2019). "The Fragmented Death of the Farallon Plate". *Geophysical research letters* 46.13, pp. 7386–7394. DOI: 10.1029/2019GL083437.

Hawley, W. B., R. M. Allen, and M. A. Richards (2016). "Tomography reveals buoyant asthenosphere accumulating beneath the Juan de Fuca Plate". *Science* 353.6306, pp. 1406–1408. DOI: 10.1126/science.aad8104.

Hyndman, R. D. and K. Wang (1993). "Thermal constraints on the zone of major thrust earthquake failure: the Cascadia subduction zone". *Journal of geophysical research: solid earth* 98.B2, pp. 2039–2060. DOI: 10.1029/92JB02279.

Janiszewski, H. A. and G. A. Abers (2015). "Imaging the plate interface in the Cascadia seismogenic zone: new constraints from offshore receiver functions". *Seismological research letters* 86.5, pp. 1261–1269. DOI: 10.1785/0220150104.

Janiszewski, H. A., J. B. Gaherty, G. A. Abers, H. Gao, and Z. C. Eilon (2019). "Amphibious surface-wave phase-velocity measurements of the Cascadia subduction zone". *Geophysical journal international* 217.3, pp. 1929–1948. DOI: 10.1093/gji/ggz051.

Jin, G. and J. B. Gaherty (2015). "Surface wave phase-velocity tomography based on multichannel cross-correlation". *Geophysical journal international* 201.3, pp. 1383–1398. DOI: 10.1093/gji/ggv079.

Kästle, E. D., R. Soomro, C. Weemstra, L. Boschi, and T. Meier (2016). "Two-receiver measurements of phase velocity: cross-validation of ambient-noise and earthquake-based observations". *Geophysical journal international* 207.3, pp. 1493–1512. DOI: 10.1093/gji/ggw341.

Levshin, A. L. and M. H. Ritzwoller (2001). "Automated detection, extraction, and measurement of regional surface waves". *Pure and applied geophysics* 158.8, pp. 1531–1545. DOI: 10.1007/978-3-0348-8264-4_11.

Lin, F.-C., M. P. Moschetti, and M. H. Ritzwoller (2008). "Surface wave tomography of the western United States from ambient seismic noise: Rayleigh and Love wave phase velocity maps". *Geophysical journal international* 173.1, pp. 281–298. DOI: 10.1111/j.1365-246X.2008.03720.x.

Lin, F.-C. and M. H. Ritzwoller (2011a). "Apparent anisotropy in inhomogeneous isotropic media". *Geophysical journal international* 186.3, pp. 1205–1219. DOI: 10.1111/j.1365-246X.2011.05100.x.

— (2011b). "Helmholtz surface wave tomography for isotropic and azimuthally anisotropic structure". *Geophysical journal international* 186.3, pp. 1104–1120. DOI: 10.1111/j.1365-246X.2011.05070.x.

Lin, F.-C., M. H. Ritzwoller, and R. Snieder (2009). "Eikonal tomography: surface wave tomography by phase front tracking across a regional broad-band seismic array". *Geophysical journal international* 177.3, pp. 1091–1110. DOI: 10.1111/j.1365-246X.2009.04105.x.

Lin, F.-C., M. H. Ritzwoller, Y. Yang, M. P. Moschetti, and M. J. Fouch (2011). "Complex and variable crustal and uppermost mantle seismic anisotropy in the western United States". *Nature geoscience* 4.1, pp. 55–61. DOI: 10.1038/ngeo1036.

Lin, F.-C., V. C. Tsai, and M. H. Ritzwoller (2012). “The local amplification of surface waves: a new observable to constrain elastic velocities, density, and anelastic attenuation”. *Journal of geophysical research: solid earth* 117.B6. DOI: 10.1029/2012JB009208.

Ma, S. and G. C. Beroza (2012). “Ambient-field Green’s functions from asynchronous seismic observations”. *Geophysical research letters* 39.6, p. L06301. DOI: 10.1029/2011GL050755.

Martin-Short, R., R. M. Allen, I. D. Bastow, E. Totten, and M. A. Richards (2015). “Mantle flow geometry from ridge to trench beneath the Gorda–Juan de Fuca plate system”. *Nature geoscience* 8.12, pp. 965–968. DOI: 10.1038/ngeo2569.

Moschetti, M. P., M. H. Ritzwoller, F.-C. Lin, and Y. Yang (2010). “Crustal shear wave velocity structure of the western United States inferred from ambient seismic noise and earthquake data”. *Journal of geophysical research* 115.B10. DOI: 10.1029/2010JB007448.

Nabelek, J. and J. Braunmiller (2012). “Plate boundary evolution and physics at an oceanic transform fault system”. International Federation of Digital Seismograph Networks. Dataset/Seismic Network. DOI: 10.7914/SN/X9_2012.

— (2013). “Seismicity, structure and dynamics of the Gorda deformation zone.” International Federation of Digital Seismograph Networks. Dataset/Seismic Network. DOI: 10.7914/SN/Z5_2013.

Nelson, A. R., B. F. Atwater, P. T. Bobrowsky, L.-A. Bradley, J. J. Clague, G. A. Carver, M. E. Darienzo, W. C. Grant, H. W. Krueger, R. Sparks, T. W. Stafford, and M. Stuiver (1995). “Radiocarbon evidence for extensive plate-boundary rupture about 300 years ago at the Cascadia subduction zone”. *Nature* 378.6555, pp. 371–374. DOI: 10.1038/378371a0.

Ritzwoller, M. H. and L. Feng (2019). “Overview of pre- and post-processing of ambient-noise correlations”. *Seismic ambient noise*. Ed. by N. Nakata, L. Gualtieri, and A. Fichtner. Cambridge: Cambridge University Press. DOI: 10.1017/9781108264808.

Ruan, Y., D. W. Forsyth, and S. W. Bell (2014). “Marine sediment shear velocity structure from the ratio of displacement to pressure of Rayleigh waves at seafloor”. *Journal of geophysical research: solid earth* 119.8, pp. 6357–6371.

— (2018). “Shear attenuation beneath the Juan de Fuca plate: Implications for mantle flow and dehydration”. *Earth and planetary science letters* 496, pp. 189–197. DOI: 10.1016/j.epsl.2018.05.035.

Rychert, C. A., N. Harmon, and S. Tharimena (2018). “Scattered wave imaging of the oceanic plate in Cascadia”. *Science advances* 4.2, eaao1908. DOI: 10.1126/sciadv.aao1908.

Sabra, K. G., P. Gerstoft, P. Roux, W. A. Kuperman, and M. C. Fehler (2005). “Surface wave tomography from microseisms in Southern California”. *Geophysical research letters* 32.14, p. L14311. DOI: 10.1029/2005GL023155.

Satake, K., K. Shimazaki, Y. Tsuji, and K. Ueda (1996). "Time and size of a giant earthquake in Cascadia inferred from Japanese tsunami records of January 1700". *Nature* 379.6562 (6562), pp. 246–249. DOI: 10.1038/379246a0.

Shapiro, N. M. and M. Campillo (2004). "Emergence of broadband Rayleigh waves from correlations of the ambient seismic noise". *Geophysical research letters* 31.7, p. L07614. DOI: 10.1029/2004GL019491.

Shapiro, N. M. and M. H. Ritzwoller (2004). "Thermodynamic constraints on seismic inversions". *Geophysical journal international* 157.3, pp. 1175–1188. DOI: 10.1111/j.1365-246X.2004.02254.x.

Shapiro, N. M., M. Campillo, L. Stehly, and M. H. Ritzwoller (2005). "High-resolution surface-wave tomography from ambient seismic noise". *Science* 307.5715, pp. 1615–1618. DOI: 10.1126/science.1108339.

Shen, W. and M. H. Ritzwoller (2016). "Crustal and uppermost mantle structure beneath the United States". *Journal of geophysical research: solid earth* 121.6, pp. 4306–4342. DOI: 10.1002/2016JB012887.

Sheng, Y., N. Nakata, and G. C. Beroza (2018). "On the nature of higher-order ambient seismic field correlations". *Journal of geophysical research: solid earth* 123.9, pp. 7969–7982. DOI: 10.1029/2018JB015937.

Smith, M. L. and F. A. Dahlen (1973). "The azimuthal dependence of Love and Rayleigh wave propagation in a slightly anisotropic medium". *Journal of geophysical research* 78.17, pp. 3321–3333. DOI: 10.1029/JB078i017p03321.

Stehly, L., M. Campillo, B. Froment, and R. L. Weaver (2008). "Reconstructing Green's function by correlation of the coda of the correlation (C^3) of ambient seismic noise". *Journal of geophysical research* 113.B11, B11306. DOI: 10.1029/2008JB005693.

Tarantola, A. (2005). *Inverse problem theory and methods for model parameter estimation*. Vol. 89. Philadelphia, PA: Society for Industrial and Applied Mathematics. 342 pp.

Tian, Y. and M. H. Ritzwoller (2015). "Directionality of ambient noise on the Juan de Fuca Plate: implications for source locations of the primary and secondary microseisms". *Geophysical journal international* 201.1, pp. 429–443. DOI: 10.1093/gji/ggv024.

— (2017). "Improving ambient noise cross-correlations in the noisy ocean bottom environment of the Juan de Fuca plate". *Geophysical journal international* 210.3, pp. 1787–1805. DOI: 10.1093/gji/ggx281.

Tian, Y., W. Shen, and M. H. Ritzwoller (2013). "Crustal and uppermost mantle shear velocity structure adjacent to the Juan de Fuca Ridge from ambient seismic noise". *Geochemistry, geophysics, geosystems* 14.8, pp. 3221–3233. DOI: 10.1002/ggge.20206.

Toomey, D., R. Allen, A. Barclay, S. Bell, P. Bromirski, R. Carlson, X. Chen, J. Collins, R. Dziak, B. Evers, D. Forsyth, P. Gerstoft, E. Hooft, D. Livelybrooks, J. Lodewyk, D. Luther, J. McGuire, S. Schwartz, M. Tolstoy, A. Trehu, M. Weirathmueller, and

W. Wilcock (2014). "The Cascadia Initiative: a sea change in seismological studies of subduction zones". *Oceanography* 27.2, pp. 138–150. DOI: 10.5670/oceanog.2014.49.

VanderBeek, B. P. and D. R. Toomey (2017). "Shallow mantle anisotropy beneath the Juan de Fuca plate". *Geophysical research letters*. DOI: 10.1002/2017GL074769.

— (2019). "Pn tomography of the Juan de Fuca and Gorda Plates: implications for mantle deformation and hydration in the oceanic lithosphere". *Journal of geophysical research: solid earth* 124.8, pp. 8565–8583. DOI: 10.1029/2019JB017707.

Webb, S. C. and W. C. Crawford (1999). "Long-period seafloor seismology and deformation under ocean waves". *Bulletin of the seismological society of america* 89.6, pp. 1535–1542.

Wilson, D. S. (1993). "Confidence intervals for motion and deformation of the Juan de Fuca Plate". *Journal of geophysical research: solid earth* 98.B9, pp. 16053–16071. DOI: 10.1029/93JB01227.

Xie, J., M. H. Ritzwoller, S. Brownlee, and B. Hacker (2015). "Inferring the oriented elastic tensor from surface wave observations: preliminary application across the western United States". *Geophysical journal international* 201.2, pp. 996–1021. DOI: 10.1093/gji/ggv054.

Xie, J., M. H. Ritzwoller, W. Shen, and W. Wang (2017). "Crustal anisotropy across eastern Tibet and surroundings modeled as a depth-dependent tilted hexagonally symmetric medium". *Geophysical journal international* 209.1, pp. 466–491. DOI: 10.1093/gji/ggx004.

Yang, Y. and M. H. Ritzwoller (2008). "Teleseismic surface wave tomography in the western U.S. using the Transportable Array component of USArray". *Geophysical research letters* 35.4. DOI: 10.1029/2007GL032278.

Zhang, S., L. Feng, and M. H. Ritzwoller (2020). "Three-station interferometry and tomography: coda versus direct waves". *Geophysical journal international* 221.1, pp. 521–541. DOI: 10.1093/gji/ggaa046.

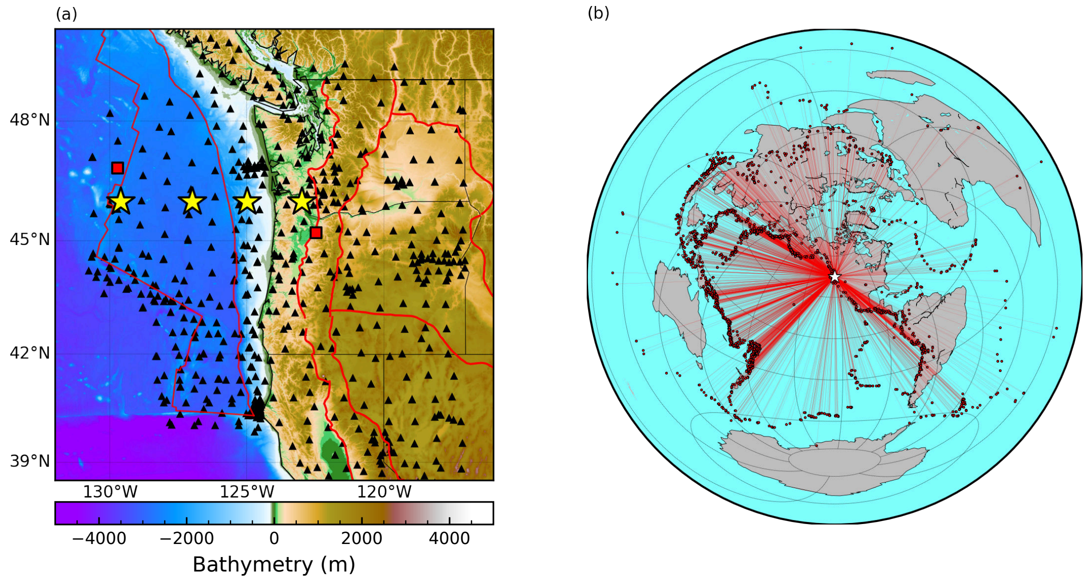

Figure 1: **Stations and earthquakes used.** (a) Region of study. Black triangles denote stations, red squares mark the pair of stations used in **Fig. 3**, and yellow stars represent example locations along 46°N referenced in **Figs 5, 14 and 17**. The background colors depict bathymetry (GEBCO Compilation Group, 2019). Red lines onshore denote physiographic provinces (Fenneman and Johnson, 1946) while red lines offshore depict plate boundaries (Bird, 2003). (b) Earthquake locations are denoted by red circles and red lines denote great circles between earthquakes and the center of the region of study (white star).

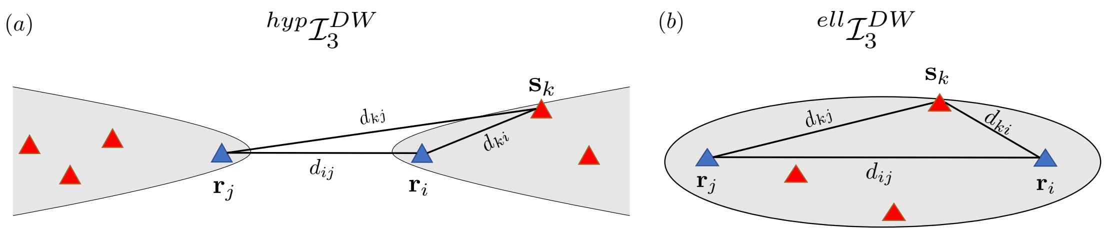

Figure 2: **Schematic representation of three-station direct-wave interferometry.** (a) For the three-station method $^{hyp}\mathcal{I}_3^{DW}$, source-stations (s_k) are constrained to lie within a hyperbolic stationary phase zone with the receiver-stations (r_i, r_j) as foci. Two-station interferograms between s_k and r_i, r_j are correlated. Great circle distances between two stations are denoted as d with appropriate subscripts. (b) Similar to (a) but for the three-station method $^{ell}\mathcal{I}_3^{DW}$, the source-stations are constrained to lie within an elliptical stationary phase zone, and the two-station interferograms between s_k and r_i, r_j are convolved.

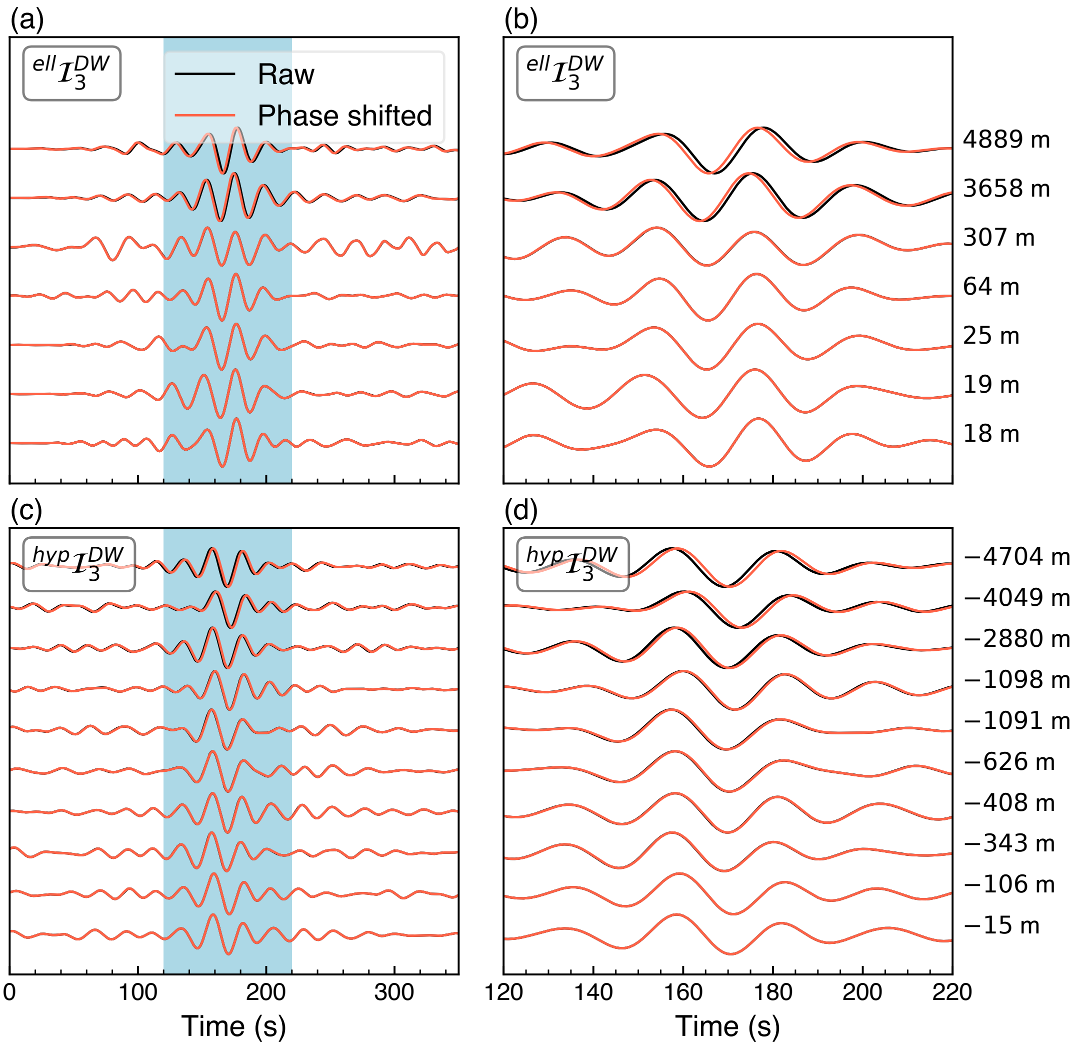

Figure 3: **De-biasing three-station direct-wave methods via phase shift.** (a) For the method $^{ell}\mathcal{I}_3^{DW}$, to de-bias we apply a phase advance to correct for δd (eq. (4)). The source-specific interferograms are shown before (C_3, in black) and after ($\tilde{C}_3$, in red) the phase shift, respectively. The shaded areas are zoomed in (b). The values of δd are listed to the right of each trace. (c) & (d) Similar to (a) & (b), for the method $^{hyp}\mathcal{I}_3^{DW}$ we de-bias by applying a phase delay (eq. (3)). The receiver-stations are 7D.J47A (WHOI OBS) and UW.LCCR (Mulino, OR), and the inter-receiver distance is 589 km (**Fig. 1a**). All traces are low-pass filtered with a corner at 20 s period to ease visualization.

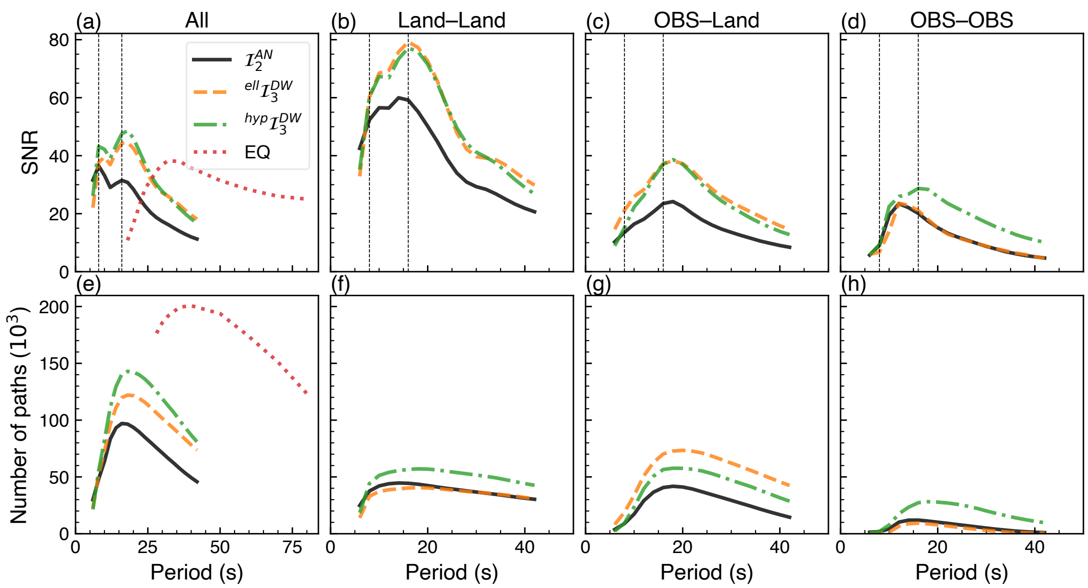

Figure 4: **Characteristics of dispersion measurements.** (a)-(d) Median of the SNR of the measurements for different methods plotted as a function of period for $\mathcal{I}_2^{AN}$ (black), ${}^{ell}\mathcal{I}_3^{DW}$ (orange), ${}^{hyp}\mathcal{I}_3^{DW}$ (green), and earthquakes (red). The median values (a) are taken over all paths, (b) are for paths between a pair of land stations, (c) are between an OBS and a land station, and (d) are between a pair of OBS. Vertical lines mark the primary (~16 s) and secondary (~8 s) microseism peaks. (e)-(h) Similar to (a)-(d) but for the number of paths after quality control. The number of paths is twice that of travel time measurements for $\mathcal{I}_2^{AN}$, ${}^{ell}\mathcal{I}_3^{DW}$ and ${}^{hyp}\mathcal{I}_3^{DW}$ while the same as travel time measurements for earthquake data. Numbers presented are in thousands.

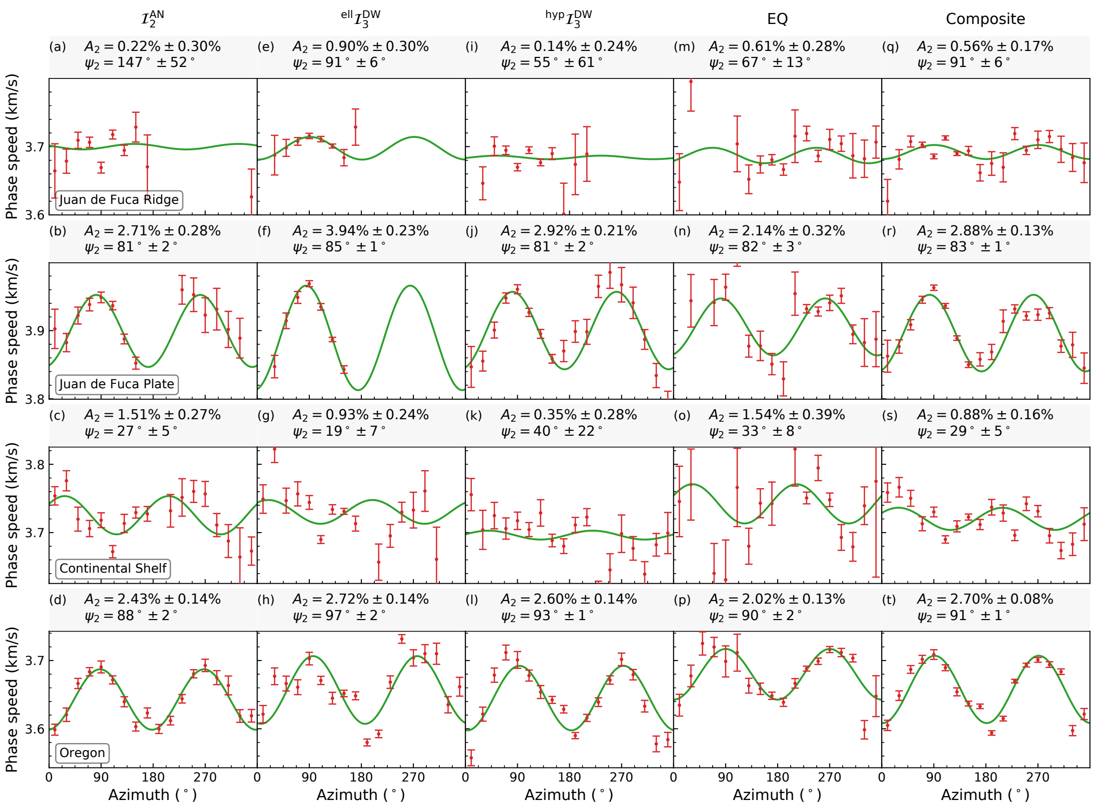

Figure 5: **Observations of azimuthal anisotropy at various locations using different methods.** Observed (red bars) and estimated (green lines) Rayleigh wave phase speed at 30 s period are plotted versus azimuth for (column 1) $\mathcal{I}_2^{AN}$, (column 2) ${}^{ell}\mathcal{I}_3^{DW}$, (column 3) ${}^{hyp}\mathcal{I}_3^{DW}$, (column 4) earthquakes, and (column 5) composite data (row 1) near the Juan de Fuca Ridge, (row 2) on the Juan de Fuca Plate, (row 3) on the continental shelf east of the Juan de Fuca Plate, and (row 4) on the continent (**Fig. 1a**). Fit parameters are above each panel for 2ψ anisotropy amplitude A_2, and 2ψ fast direction ψ_2 (eq. (12)).

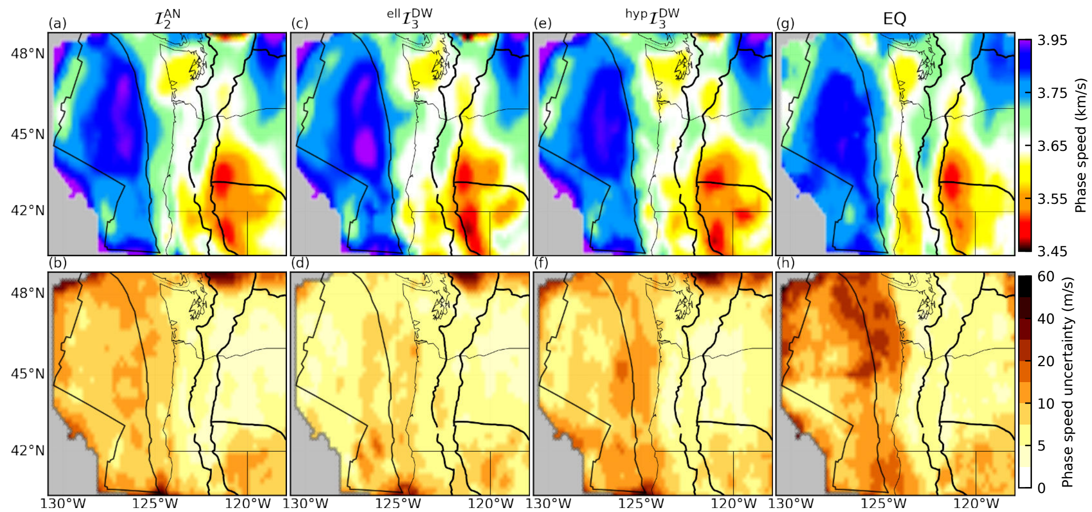

Figure 6: **Rayleigh wave phase speed maps at 30 s period from different methods.** (a) Phase speed map $\bar{c}$ using $\mathcal{I}_2^{AN}$and (b) associated uncertainties $\sigma_{\bar{c}}$. (c)-(h) Similar to (a) & (b) except based on (c) & (d) ${}^{ell}\mathcal{I}_3^{DW}$, (e) & (f) ${}^{hyp}\mathcal{I}_3^{DW}$, and (g) & (h) earthquakes (EQ).

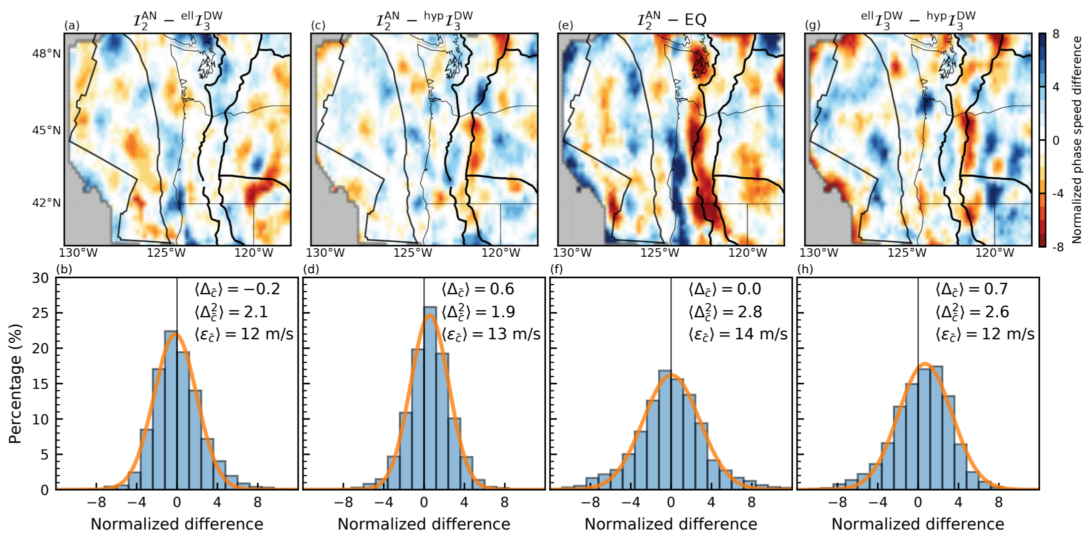

Figure 7: **Normalized differences between 30 s Rayleigh wave isotropic phase speed maps (Fig. 6) from different methods.** (a) Normalized difference $\Delta_{\bar{c}}$ (eq. 14) between results from $\mathcal{I}_2^{AN}$and ${}^{ell}\mathcal{I}_3^{DW}$. (b) Histogram taken over the spatial nodes of (a). The orange line denotes a Gaussian fit to the histogram. The spatial mean $\langle\Delta_{\bar{c}}\rangle$ and standard deviation $\langle\Delta^2_{\bar{c}}\rangle$ of $\Delta_{\bar{c}}$, and the spatial mean of the combined uncertainties $\langle\epsilon_{\bar{c}}\rangle$ (eq. 13) are listed on the upper right corner. (c)-(h) Similar to (a) & (b) except the comparison in (c) & (d) is based on ${}^{hyp}\mathcal{I}_3^{DW}$and $\mathcal{I}_2^{AN}$, in (e) & (f) it is based on earthquake data (EQ) and $\mathcal{I}_2^{AN}$, and in (g) & (h) it is based on ${}^{ell}\mathcal{I}_3^{DW}$and ${}^{hyp}\mathcal{I}_3^{DW}$.

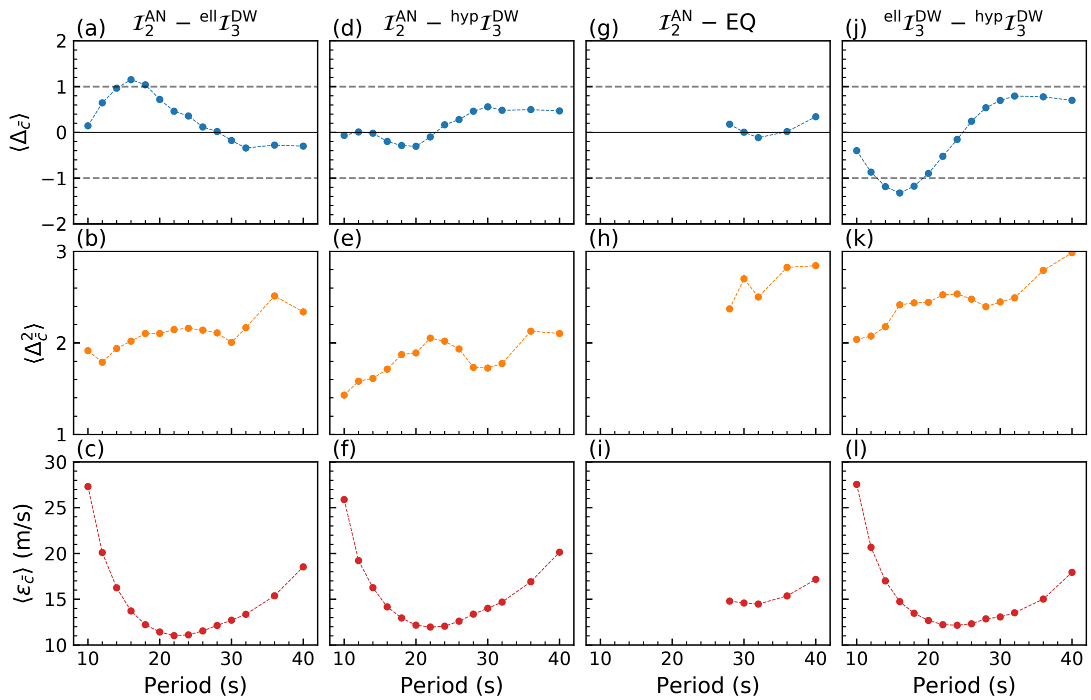

Figure 8: **Statistics of period-dependent differences between the isotropic phase speed maps from different methods.** (a) & (b) The differences are spatial means $\langle\Delta_{\bar{c}}\rangle$ and standard deviations $\langle\Delta_{\bar{c}}^2\rangle$ of the normalized difference $\Delta_{\bar{c}}$ (eq. 14) between $\mathcal{I}_2^{AN}$and ${}^{ell}\mathcal{I}_3^{DW}$, with (c) associated spatial mean of combined uncertainties $\langle\epsilon_{\bar{c}}\rangle$ (eqs. (14)–(16)). (d)-(l) Similar to (a) - (c) except the comparison in (d) - (f) is based on ${}^{hyp}\mathcal{I}_3^{DW}$and $\mathcal{I}_2^{AN}$, in (g) - (i) it is based on earthquake data (EQ) and $\mathcal{I}_2^{AN}$, and in (j) & (l) it is based on ${}^{ell}\mathcal{I}_3^{DW}$and ${}^{hyp}\mathcal{I}_3^{DW}$.

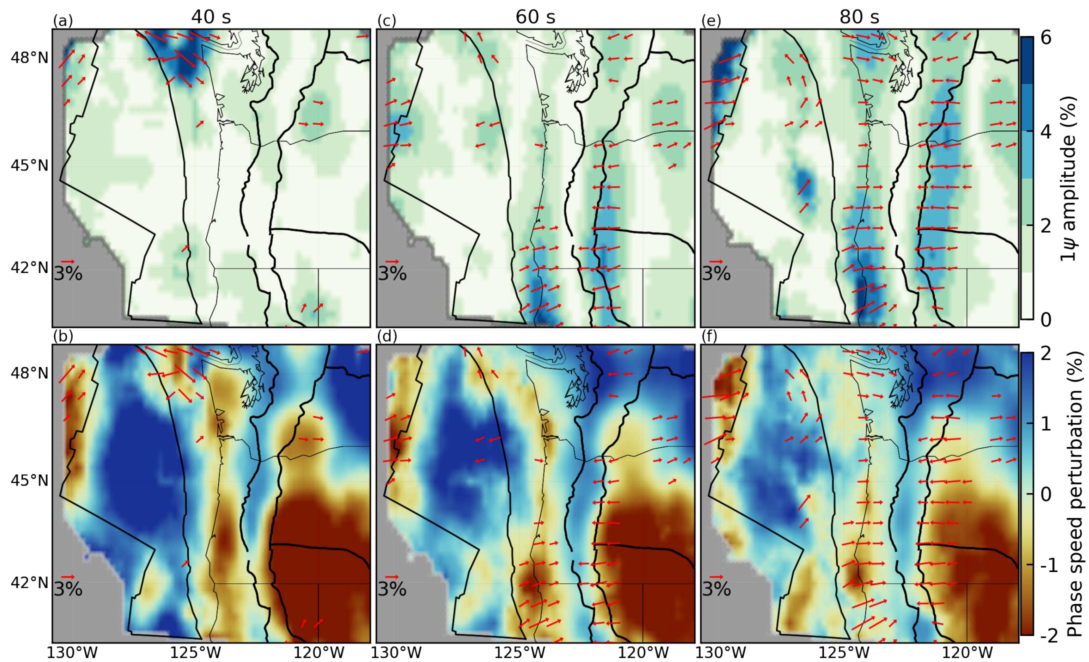

Figure 9: **Observation of apparent 1ψ azimuthal anisotropy.** (a) & (b) At 40 s period, (a) the red arrows point in the fast direction of 1ψ anisotropy, ψ_1, with lengths proportional to the peak-to-peak 1ψ amplitudes, A_1 (eq. (12)). The arrows are drawn only where $A_1 > 2\%$. The background map depicts A_1. (b) The arrows are the same as in (a) but the background map depicts the isotropic phase speed A_0. (c)-(f) Similar to (a) & (b) but at (c) & (d) 60 s period and (e) & (f) 80 s period.

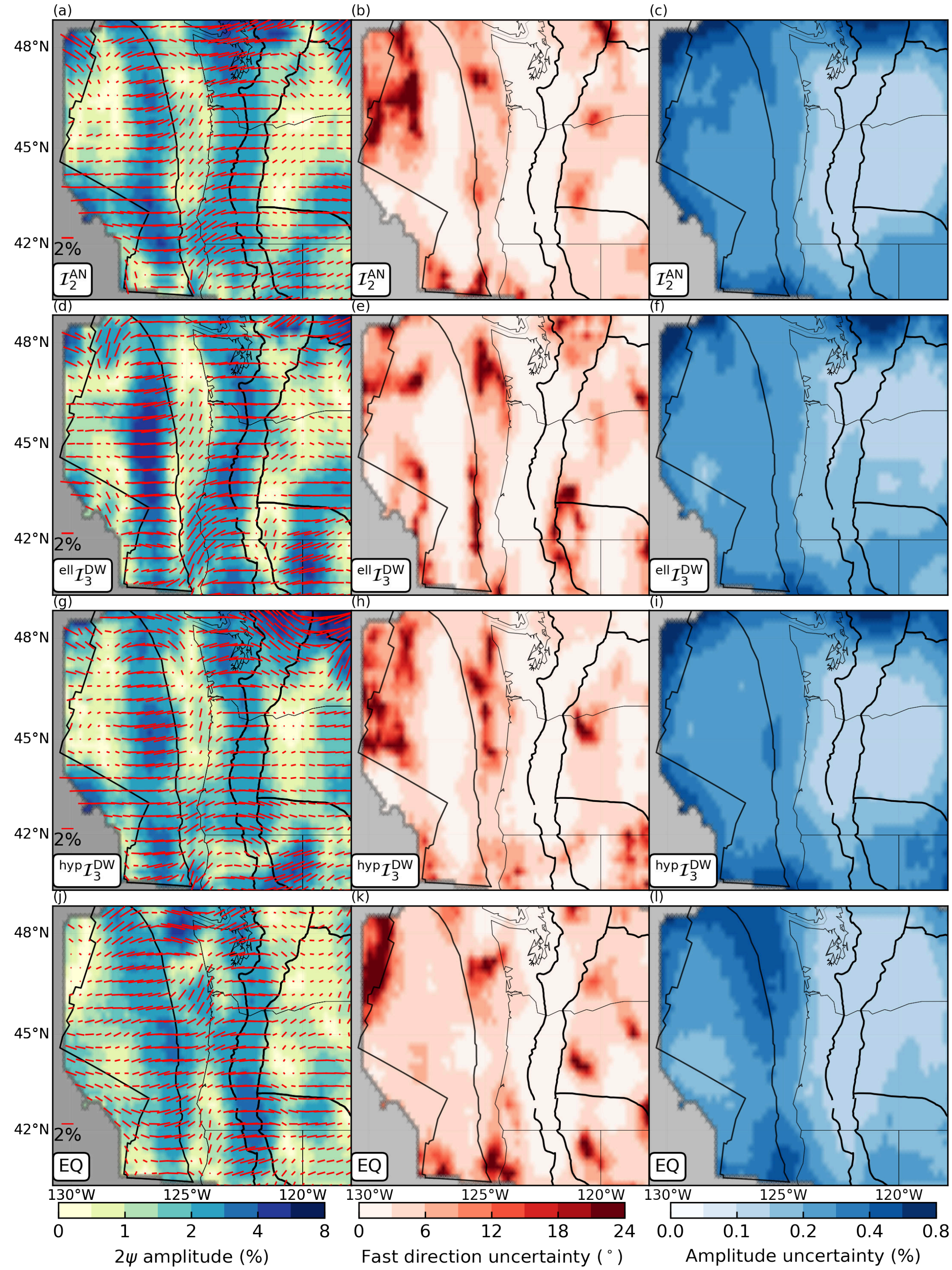

Figure 10: **Rayleigh wave 2ψ azimuthal anisotropy maps at 30 s period from different methods.** (a)-(c) Based on $\mathcal{I}_2^{AN}$, (a) 2ψ peak-to-peak amplitudes A_2 (eq. (12)) and fast directions ψ_2 are represented by the lengths and directions of red bars, respectively. The background map depicts A_2. The associated uncertainties are shown for (b) ψ_2 and (c) A_2. (d)-(l) Similar to (a)-(c) except based on (d)-(f) $^{ell}\mathcal{I}_3^{DW}$, (g)-(i) $^{hyp}\mathcal{I}_3^{DW}$, and (j)-(l) earthquake data.

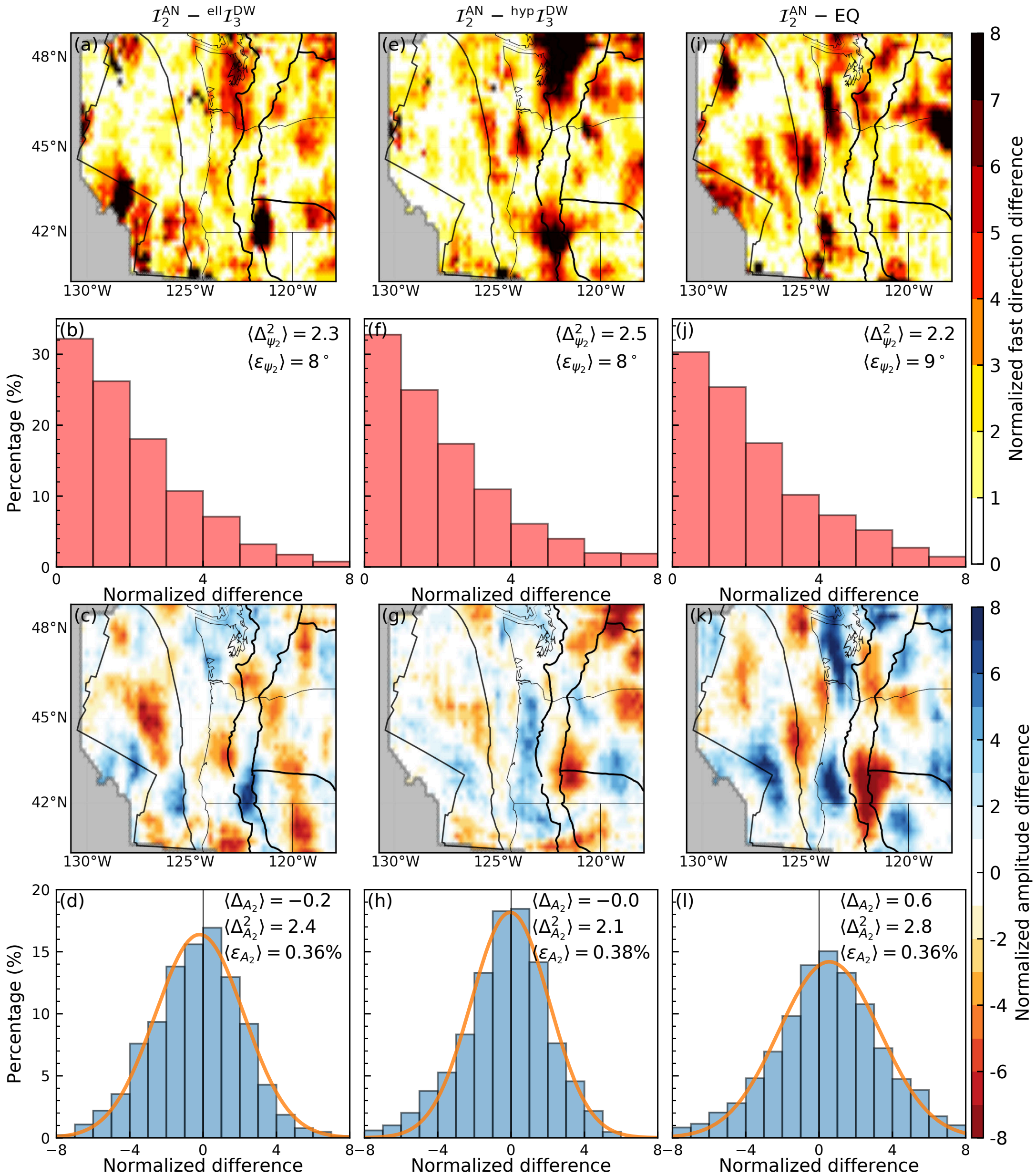

Figure 11: **Comparison of the 30 s period Rayleigh wave 2ψ azimuthal anisotropy maps (Fig. 10) based on different methods.** (a) Normalized absolute difference of 2ψ fast directions (Δ_{ψ_2}) between $\mathcal{I}_2^{AN}$ and ${}^{ell}\mathcal{I}_3^{DW}$. (b) Histogram of (a). The spatial standard deviation of the normalized difference $\langle\Delta^2_{\psi_2}\rangle$ and the spatial mean of the combined uncertainties $\langle\epsilon_{\psi_2}\rangle$ are listed in the upper right corner. (c) & (d) Similar to (a) & (b) except the difference is for 2ψ amplitudes, A_2. The orange line in (d) is the Gaussian fit to the histogram and the spatial mean of the normalized difference $\langle\Delta_{A_2}\rangle$ is also listed. (e)-(l) Similar to (a)-(d), except the difference is (e)-(h) between $\mathcal{I}_2^{AN}$ and ${}^{hyp}\mathcal{I}_3^{DW}$, and (i)-(l) between $\mathcal{I}_2^{AN}$ and earthquake data (EQ).

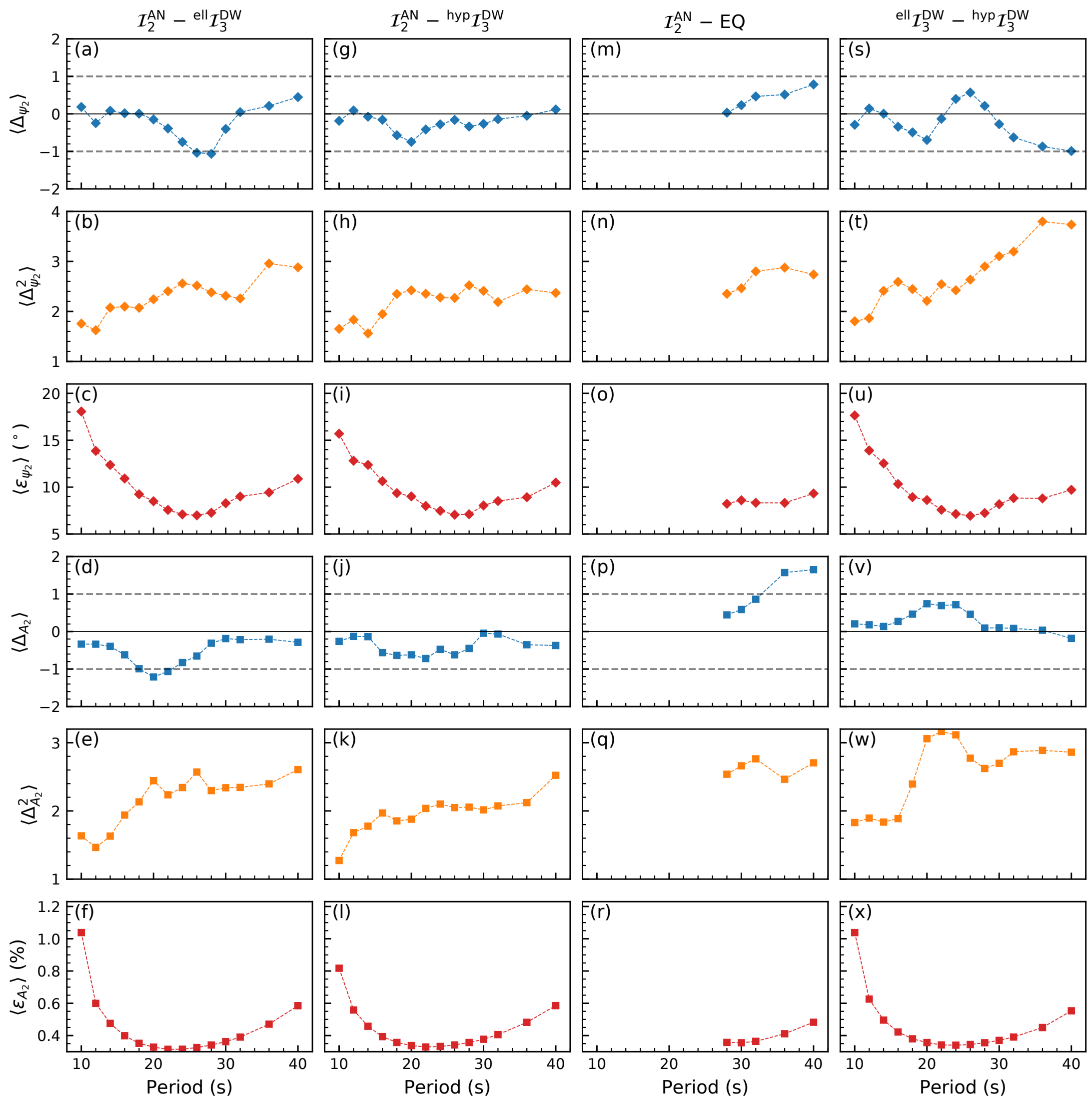

Figure 12: **Statistics of period-dependent differences between the anisotropic maps from different methods.** (a)-(c) The statistics are spatial (a) means $\langle\Delta_{\psi_2}\rangle$ and (b) standard deviations $\langle\Delta^2_{\psi_2}\rangle$ of the normalized difference in fast directions Δ_{ψ_2} (eq. (14)) between $\mathcal{I}_2^{AN}$and ${}^{ell}\mathcal{I}_3^{DW}$, and (c) is the associated spatial mean of combined uncertainties $\langle\epsilon_{\psi_2}\rangle$. (d)-(f) Similar to (a)-(c) except the statistics are for amplitudes A_2. (g)-(x) Similar to (a)-(f) except in (g)-(l) the comparison is based on ${}^{hyp}\mathcal{I}_3^{DW}$and $\mathcal{I}_2^{AN}$, in (m)-(r) it is based on earthquake data (EQ) and $\mathcal{I}_2^{AN}$, and in (s)-(x) it is based on ${}^{ell}\mathcal{I}_3^{DW}$and ${}^{hyp}\mathcal{I}_3^{DW}$.

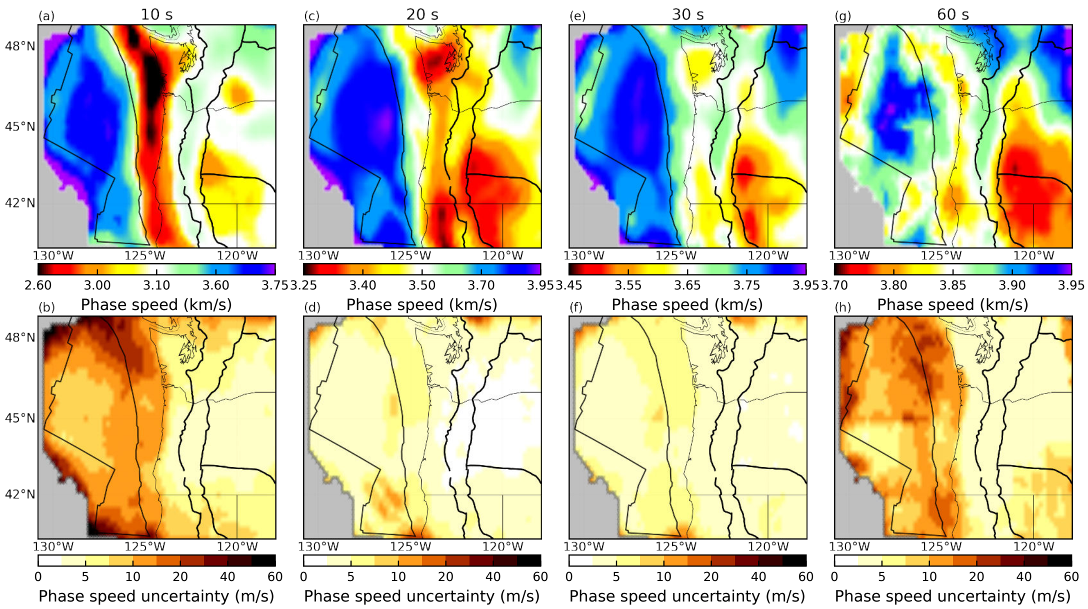

Figure 13: **Composite Rayleigh wave isotropic phase speed maps at several periods.** (a) Phase speed map $\bar{c}$ at 10 s period combining data from $\mathcal{I}_2^{AN}$, ${}^{ell}\mathcal{I}_3^{DW}$ and ${}^{hyp}\mathcal{I}_3^{DW}$ with (b) associated uncertainties $\sigma_{\bar{c}}$. (c) & (d) Similar to (a) & (b) except at 20 s period. (e) & (f) Similar to (a) & (b) except at 30 s period. At this period, earthquake data also contribute. (g) & (h) Similar to (a) & (b) except at 60 s period where only earthquake data are available.

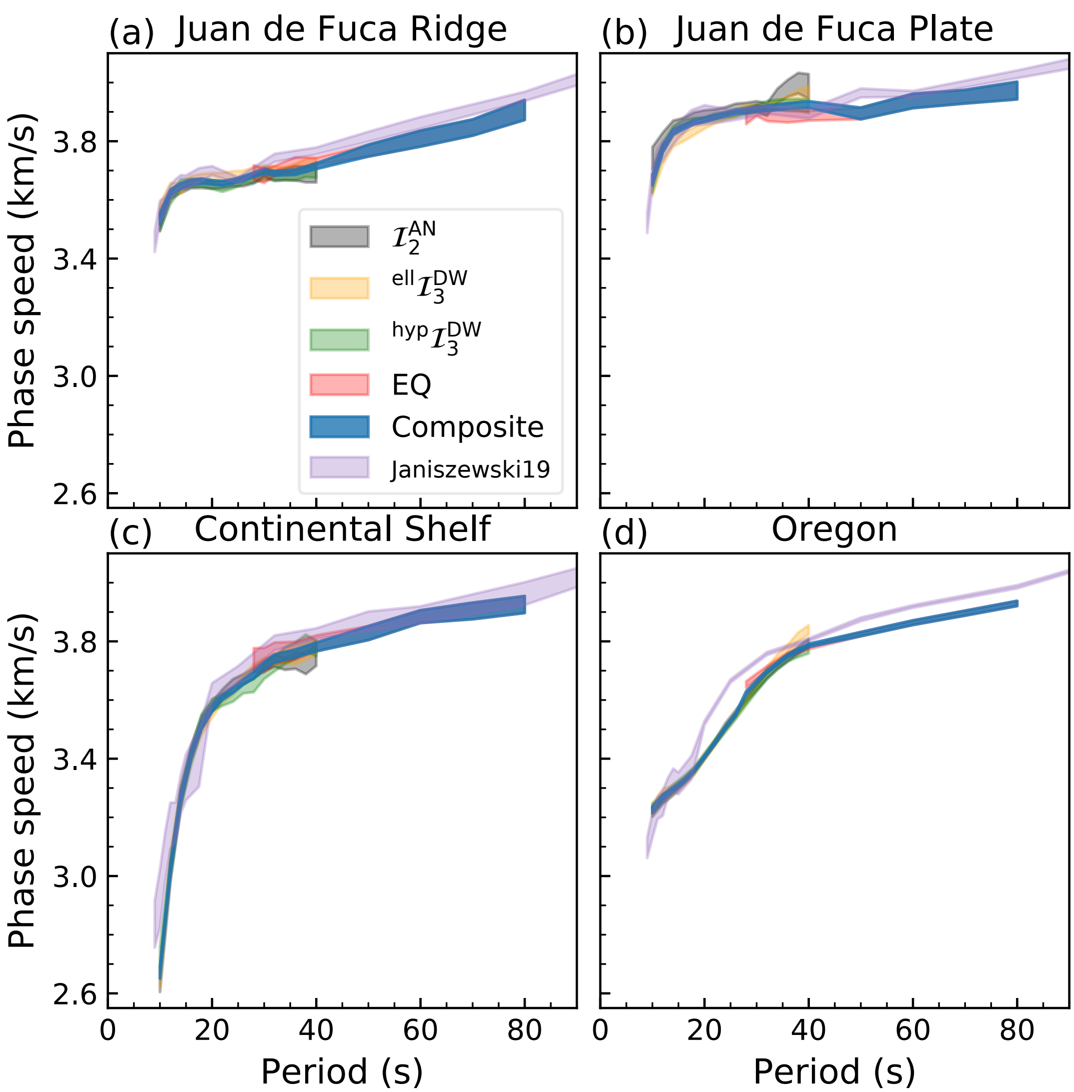

Figure 14: **Local Rayleigh wave isotropic dispersion curves.** Local dispersion curves are plotted from (a) near the Juan de Fuca Ridge, (b) on the Juan de Fuca Plate, (c) on the continental shelf, and (d) on the continent (**Fig. 1a**) from $\mathcal{I}_2^{AN}$(gray), ${}^{ell}\mathcal{I}_3^{DW}$(red), ${}^{hyp}\mathcal{I}_3^{DW}$(green), earthquake data (orange), composite data (blue), and Janiszewski et al. (2019) (light purple). The shadings represent $\bar{c} \pm 2\sigma_{\bar{c}}$.

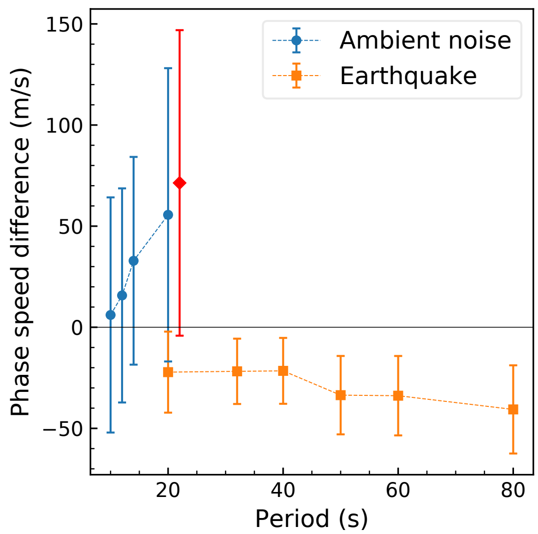

Figure 15: **Comparison of isotropic phase speed maps with those from Janiszewski et al. (2019).** Error bars denote the spatial mean of the raw difference $\pm$ combined uncertainties $\langle \epsilon_{\bar{c}} \rangle$. Maps of Janiszewski et al. (2019) are from ambient noise at periods $\leq$ 20 s (blue circles) and from earthquake data at periods $\geq$ 20 s (orange squares). The red error bar is the difference between their ambient noise and earthquake results at 20 s (slightly shifted from 20 s for visualization). These results can be compared approximately to differences in the maps produced by our methods by multiplying $\langle \Delta_{\bar{c}} \rangle$ and $\langle \epsilon_{\bar{c}} \rangle$ from **Fig. 8**.

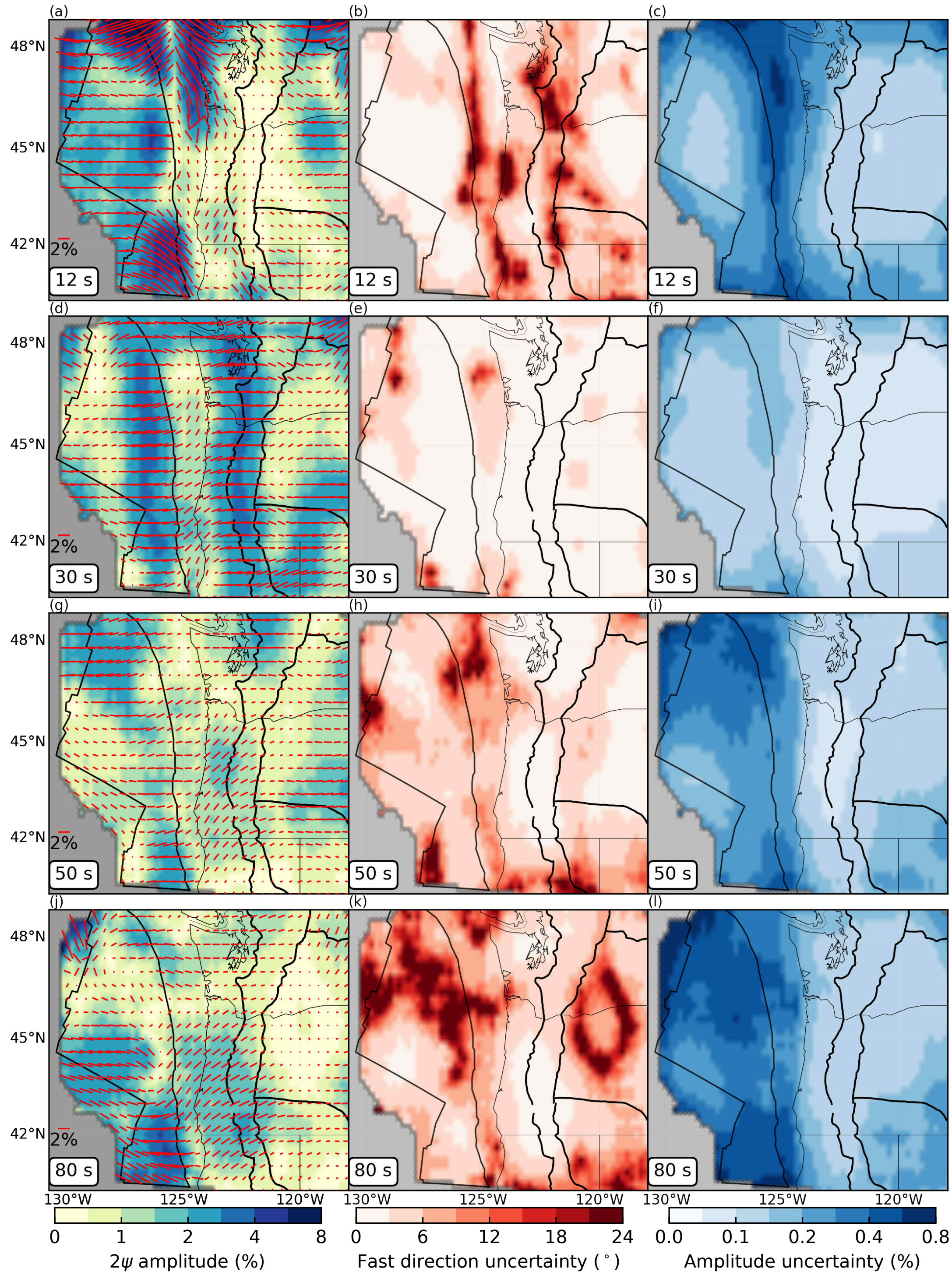

Figure 16: **Composite 2ψ azimuthal anisotropy maps at several periods.** (a)-(c) Similar to **Figs 10a-c** but based on combined data from $\mathcal{I}_2^{AN}$, ${}^{ell}\mathcal{I}_3^{DW}$ and ${}^{hyp}\mathcal{I}_3^{DW}$ at 12 s period. (d)-(f) Similar to (a)-(c) except at 30 s period earthquake data are also available. (g)-(l) Similar to (a)-(c) except (g)-(i) at 50 s period and (j)-(l) at 80 s period, only earthquake data are available.

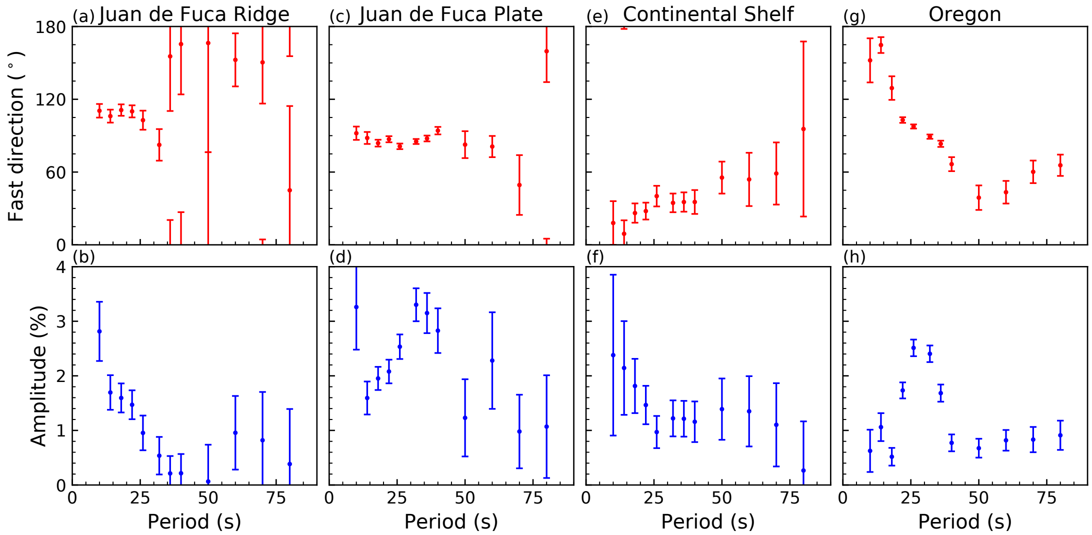

Figure 17: **Local period-dependent Rayleigh wave azimuthally anisotropic dispersion curves.** (a) Fast directions and (b) peak-to-peak amplitudes for 2ψ anisotropy versus period near the Juan de Fuca Ridge. Error bars are the mean $\pm$ twice the uncertainties: $\psi_2 \pm 2\sigma_{\psi_2}$ and $A_2 \pm 2\sigma_{A_2}$. Only earthquake data are available at periods > 40 s. (c)-(h) Similar to (a) & (b) except (c) & (d) on the Juan de Fuca Plate, (e) & (f) on the continental shelf east of the Juan de Fuca Plate, and (g) & (h) on the continent (**Fig. 1a**).